REPORT DOCUMENTATION PAGE

Public reporting burden for this collection of information is estimated to average 1 hour per response, including the time for reviewing in data needed, and completing and reviewing this collection of information. Send comments regarding this burden estimate or any other ↓ this burden to Department of Defense, Washington Headquarters Services, Directorate for Information Operations and Reports (0704-0188), 1215 Jefferson Davis Highway, Su... 4302. Respondents should be aware that notwithstanding any other provision of law, no person shall be subject to any penalty for failing to comply with a collection of information if it does not display a currently valid OMB control number. **PLEASE DO NOT RETURN YOUR FORM TO THE ABOVE ADDRESS.**

1. REPORT DATE *(DD-MM-YYYY)* 03-28-2007	2. REPORT TYPE FINAL TECHNICAL	3. DATES COVERED *(From - To)* 01/01/2004-12/31/2006

4. TITLE AND SUBTITLE	5a. CONTRACT NUMBER
DIRECT NUMERICAL SIMULATION AND EXPERIMENTAL VALIDATION OF HYPERSONIC BOUNARY-LAYER RECEPTIVITY AND INSTABILITY	5b. GRANT NUMBER FA9550-04-1-0029
	5c. PROGRAM ELEMENT NUMBER

6. AUTHOR(S) XIAOLIN ZHONG	5d. PROJECT NUMBER
	5e. TASK NUMBER
	5f. WORK UNIT NUMBER

7. PERFORMING ORGANIZATION NAME(S) AND ADDRESS(ES) UNIVERSITY OF CALIFORNIA, LOS ANGELES MECHANICAL AND AEROSPACE ENGINEERING DEPARTMENT 46-147C ENGINEERING IV BLDG. 420 WESTWOOD PLAZA LOS ANGELES, CA 90095	8. PERFORMING ORGANIZATION REPORT NUMBER

9. SPONSORING / MONITORING AGENCY NAME(S) AND ADDRESS(ES) AIRFORCE OFFICE OF SCIENTIFIC RESEARCH, AFOSR/NA DIRECTORATE OF AEROSPACE SCIENCE 4015 WILSON BLVD. RM 713 ARLINGTON VA 22203-1954	10. SPONSOR/MONITOR'S ACRONYM(S)
	11. SPONSOR/MONITOR'S REPORT NUMBER(S)

12. DISTRIBUTION / AVAILABILITY STATEMENT

APPROVED FOR PUBLIC RELEASE
DISTRIBUTION IS UNLIMITED

13. SUPPLEMENTARY NOTES

14. ABSTRACT

The objective of this research project is to compare our numerical simulation solutions with available experimental or theoretical results on hypersonic boundary layer receptivity and stability; and to conduct extensive DNS studies on the flow mechanisms of hypersonic boundary layer receptivity and stability. During the three-year period, we have conducted extensive DNS studies on the receptivity of hypersonic boundary layer flows over a sharp wedge, a flat plate, a blunt cone, and the FRESH aeroshell. DNS studies are compared with Stetson's 1984 stability experiment on Mach 7.99 flow over a blunt cone, and Maslov's leading-edge receptivity experiment on Mach 5.92 flow over a flat plate. Our numerical studies have been validated to be of high accuracy and led to further understanding of hypersonic boundary layer receptivity mechanism. Such understanding can lead to better tool for the prediction and control of high-speed boundary layer transition.

15. SUBJECT TERMS
HYPERSONIC BOUNDARY LAYER, RECEPTIVITY, STABILITY, TRANSITION, DIRECTION NUMERICAL SIMULATION, HIGH-ORDER IMMERSED INTERFACE METHOD

16. SECURITY CLASSIFICATION OF:			17. LIMITATION OF ABSTRACT	18. NUMBER OF PAGES	19a. NAME OF RESPONSIBLE PERSON XIAOLIN ZHONG
a. REPORT	b. ABSTRACT	c. THIS PAGE	UL		19b. TELEPHONE NUMBER *(include area code)* (310) 825-2905

Standard Form 298 (Rev. 8-98)
Prescribed by ANSI Std. Z39.18

FINAL TECHNICAL REPORT

DIRECT NUMERICAL SIMULATION AND EXPERIMENTAL VALIDATION OF HYPERSONIC BOUNDARY-LAYER RECEPTIVITY AND INSTABILITY

(01/01/2004 to 12/31/2006)

Xiaolin Zhong
Professor
Mechanical and Aerospace Engineering Department
University of California, Los Angeles
Los Angeles, California 90095-1597
phone: (310) 825-2905
e-mail: xiaolin@seas.ucla.edu

20070503427

Contents

1 SUMMARY

Supported by AFOSR, our previous direct numerical simulation (DNS) studies from December 1999 to November 2002 have demonstrated that our unique high-order shock fitting simulation approach is a powerful tool in studying supersonic and hypersonic boundary-layer stability and transition physics. However, experimental validation of numerical simulation methods for hypersonic boundary layer stability and transition has not been done and is urgently needed. The objective of this research project is to compare our numerical simulation solutions with available experimental or theoretical results on hypersonic boundary layer receptivity and stability; and to conduct extensive DNS studies on the flow mechanisms of hypersonic boundary layer receptivity and stability. During the three-year period, we have conducted extensive DNS studies on the receptivity of hypersonic boundary layer flows over a sharp wedge, a flat plate, a blunt cone, and the FRESH aeroshell. DNS studies are compared with Stetson's 1984 stability experiment on Mach 7.99 flow over a blunt cone, and Maslov's leading-edge receptivity experiment on Mach 5.92 flow over a flat plate. We also collaborate with Prof. Tumin in University of Arizona to compare numerical and theoretical results on receptivity of a Mach 8 flow over a sharp wedge to wall blowing-suction, and to deeply analyze the receptivity characteristics. Our numerical studies have been validated to be of high accuracy and led to further understanding of hypersonic boundary layer receptivity mechanism. Such understanding can lead to better tool for the prediction and control of high speed boundary layer transition.

The main research contributions are:

1. We have conducted DNS studies on the receptivity of a Mach 8.0 flow over a sharp wedge of a half-angle of 5.3° to wall blowing-suction. The results show that Mode F, mode S, and acoustic modes are simultaneously excited by wall blowing-suction disturbances. It is found that the frequency of the blowing-suction actuator has a significant effect on the receptivity process owing to the frequency dependence of the synchronization point between mode F and mode S. Furthermore, the excitation of mode S is strongly affected by profile and length of the forcing actuator. All cases of numerical simulations consistently show that the synchronization point plays an important role in the excitation of mode S by wall blowing-suction, i.e., mode S is strongly excited only when the blowing-suction actuator is located upstream of the synchronization point. When the forcing actuator is downstream of the synchronization point, there is very little excitation of mode S, despite the fact that the blowing-suction actuator is still located within the unstable region of mode S.

2. We collaborated with Prof. Tumin in University of Arizona to compare numerical and theoretical results on receptivity of the Mach 8 flow over a sharp wedge to wall blowing-suction, and to deeply analyze the receptivity characteristics. The perturbation flow field downstream of the blowing-suction actuator was decomposed into boundary-layer wave modes with the help of the biorthogonal eigenfunction system. It was shown that amplitudes of boundary-layer wave modes calculated with the help of the theoretical receptivity model had good agreements with

3

those obtained by projecting the numerical results onto the boundary-layer wave modes.

3. We have studied the receptivity of a Mach 5.92 over a flat plate to various two-dimensional wall perturbations: oscillation, blowing-suction, and temperature perturbation. The numerical results show that all types of two-dimensional wall perturbations eventually result in the same type of instability wave (mode S) in the boundary layer. The hypersonic boundary-layer flow is most sensitive to wall blowing-suction and least sensitive to wall temperature perturbation. It is noticed that the profile of temperature perturbation has a strong effect on receptivity process. The receptivity of the hypersonic boundary layer to temperature perturbation is proportional to the energy introduced to the steady base flow, where the energy is determined by the profile of temperature perturbation.

4. We have conducted DNS studies on the transient growth phenomena of a Mach 5.92 flat-plate boundary layer and a Mach 7.99 flow over a blunt cone to small-scale three-dimensional stationary roughness element. The surface roughness is periodic in spanwise direction. Effect of thermal flat plate boundary conditions on the receptivity process is considered by comparing numerical simulations on adiabatic and isothermal flat plates, respectively. The numerical results show that counter rotating streamwise vortices are excited by stationary roughness element. The temperature increases in the wake region of roughness peak whereas it decreases in the wake region of roughness valley. Furthermore, the speed of wake from roughness peak is slower than that from roughness valley. All these results are consistent with those of Tumin's theoretical analysis. It is also concluded based on the numerical results that the roughness element on adiabatic flat plate is more efficient in the excitations of streamwise vortices and transient growth.

5. We developed a new high-order immersed interface method for computing boundary layer transition with surface roughness. The work was motivated by discussions among the participants in the Transition Study Group Open Forum Held in the AIAA meeting in Reno in January 2005. It was pointed out that that there is a need to compute boundary layer stability and transient growth with distributive surface roughness. The new method can be arbitrarily high-order accuracy in the whole flow field, including the interface with discontinuity, and it can be useful for the simulations of transient growth to finite or nonlinear surface roughness.

2 RESEARCH OBJECTIVES

The prediction of laminar-turbulent transition in supersonic and hypersonic boundary layers is a critical part of the aerodynamics and heating analyses for the development of hypersonic transportation vehicles and re-entry vehicles. The key for an accurate transition prediction is the understanding of the physical mechanisms that lead to transition. However, many important physical mechanisms leading to hypersonic boundary layer transition are currently still not well understood. Among them, receptivity, which can provide the missing link between environment disturbances and boundary layer instability growth and transition, is currently poorly understood.

Due to the difficulties in conducting hypervelocity experiments and the complexity of hypersonic flows, fundamental hypersonic studies increasingly rely on the use of DNS as a research tool. In recent years, DNS has become a powerful tool in the studies of the stability and receptivity of supersonic and hypersonic boundary layers.

Supported by AFOSR, we have developed high-order shock-fitting DNS methods [1], which can be directly applied to hypersonic boundary layers over realistic blunt bodies with the effects of nose bluntness, the presence of bow shock waves, and the real-gas effects at high temperatures. In the past several years, we have studied the receptivity and stability of a number of 2-D and 3-D hypersonic flows over sharp wedges [2, 3], .flat plates [4, 5], and blunt cones [6-8].

The main **objectives** of this research are to compare our numerical simulation solutions with available experimental or theoretical results on hypersonic boundary layer receptivity and stability, and to conduct extensive DNS studies on the flow mechanisms of hypersonic boundary layer receptivity and stability. The DNS numerical tools, as well as other theoretical approaches such as the linear stability analysis and the modal decomposition of biorthogonal eigenfunction system, are used to gain new fundamental understandings of receptivity and stability of hypersonic boundary layers. The goal of these studies is to lead to a better understanding of validity, accuracy, and limitation of DNS results through experimental and theoretical comparisons, and to achieve new improvements on the prediction tools for hypersonic boundary layer transition, by incorporating the effects of forcing disturbances.

Six major research tasks have been undertaken in this research project. They are:

A) Code validation of Stetson's stability experiment of Mach 7.99 flow over a blunt cone [9];
B) Receptivity to wall blowing-suction of a Mach 8 flow over a sharp wedge;
C) Receptivity to various two-dimensional wall perturbations of the flat-plate boundary layer flow corresponding to Maslov et al.'s leading-edge receptivity experiments [10];
D) Roughness induced transient growth in a Mach 7.99 flow over a blunt cone and the Mach 5.92 flat-plate boundary layer;
E) Development of a new high-order immersed interface method [11, 12] for the simulations of transient growth to finite or nonlinear surface roughness;
F) Stability and receptivity of hypersonic flow over the FRESH areoshell.

The main approach is to use DNS as a research tool to study hypersonic boundary layer receptivity physics. Linear stability analysis (LST) and model decomposition of biorthogonal eigenfunction system are used in conjunction with DNS to help better understand the flow instability mechanisms in numerical solutions. Our fifth-order upwind finite difference shock fitting method [13] for the DNS of hypersonic flows with a strong bow shock is used. The use of the high-order shock-fitting scheme makes it possible to obtain highly accurate mean flow and unsteady solutions, which are free of spurious numerical oscillations behind the bow shock.

3   RESEARCH ACCOMPLISHMENTS

The research project described in the previous section was carried out in a three period from January 1, 2004 to January 1, 2007. The three-year research project supported by this grant has led to the publications of

1. **Nine** papers in the archive journals or book chapters,
2. **Thirteen** conference papers (mainly AIAA papers),
3. **One** Ph.D. thesis by a student who has graduated with his Ph.D. degree.

More importantly, the research has produced a large amount of new results, and has led to new understanding of a number of hypersonic boundary layer receptivity mechanisms. The understanding of the receptivity process is the key to improve current hypersonic boundary layer transition prediction methods. In the following sections, the major research accomplishments are summarized, followed by a more details discussions of some of our new results in hypersonic boundary layer receptivity.

3.1 Code validation of Stetson's stability experiment of Mach 7.99 flow over a blunt cone

Publications: [4], [15], [18]

We have carried out code validation for the Stetson's stability experiment of Mach 7.99 flow over a blunt cone. The simulation results for the second mode growth compared well with those of the experiments and LST. The receptivity to wall blowing/suction at three different surface locations is used to excite the second mode instability waves in the numerical simulation of the full Navier-Stokes equations. It is found (Fig. 1) that the experimental second-mode amplitude growth ratios, N factors, and growth rates agree well with those of the simulation in a linear growth region of $195<s<215$ for frequencies near the peak second mode instability. It is concluded that the simulation and LST are accurate in predicting second mode growth in the current hypersonic boundary layer flows.
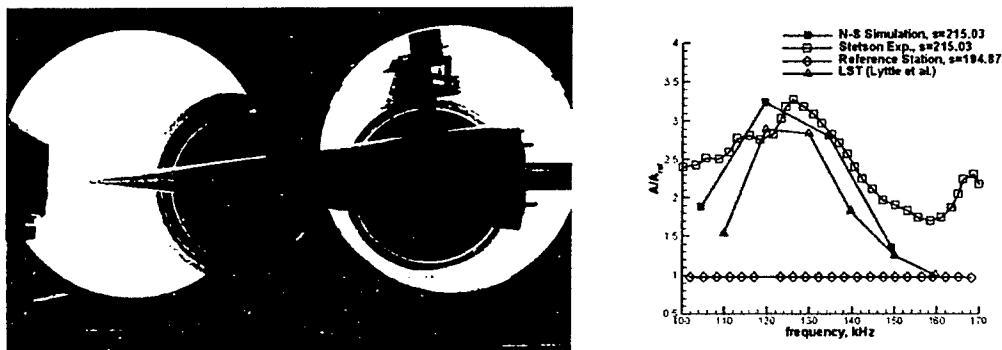

Fig. 1 The 7° half-angle blunt cone of Stetson's Mach 7.99 stability experiments [9] and numerical simulation of second mode growth by surface blowing/suction at surface station of 215 nose radii.
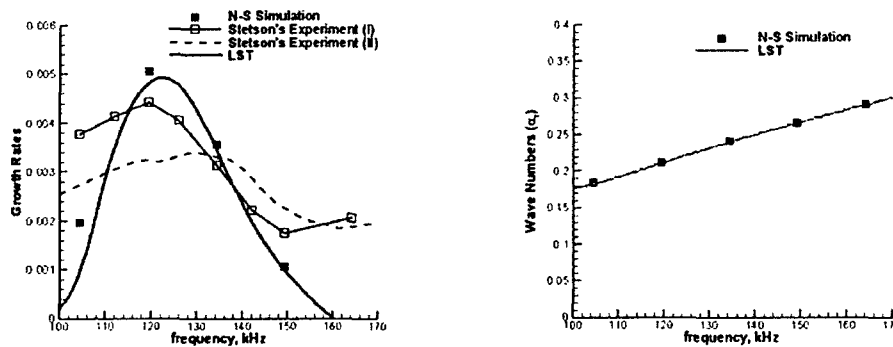
Fig. 2 Experimental, simulation and LST comparison of growth rates, wave numbers, and amplitude ratios (using 195 surface location as reference) at surface station of s = 215.

Fig. 2 compares the second mode growth rates, and wave numbers at the surface station of s=215. Two sets of experimental growth rates of Stetson are plotted. The first set (labeled as Stetson's Experiment II in the figure) is the growth rates published in Stetson's original 1984 paper. The second set (Stetson's Experiment I) are those calculated by the current author based on the new published experimental results (Fig. 28 of Schneider's review paper [14]). The growth rates of the current simulation of four frequencies are plotted in the figure. These four frequencies show second mode excitation at this location in the simulation results. This figure shows that the growth rates of the full Navier-Stokes simulation agree very well with the LST results. On the other hand, the newly published experimental growth rates are much closer to those of the original LST and experimental results with a 3% difference in wave number and a 12% difference in growth rate for the peak growth rate. This is a reasonable agreement considering the fact that the wall surface is not perfectly adiabatic in the experiment.

3.2 Receptivity to wall blowing-suction of a Mach 8 flow over a sharp wedge

Publications: [3], [7], [14], [16], [21]

Understanding the receptivity process is of critical importance to the prediction and control of boundary layer transition. With the development of advanced computers and numerical techniques, numerical simulation of the receptivity process by directly solving Navier-Stokes equations has become feasible. By solving the compressible linearized Navier-Stokes equations, Malik et al. [15] investigated the responses of a Mach 8 flow over a sharp wedge of a half-angle of $5.3°$ to three types of external forcing: a planar free-stream acoustic wave, a narrow acoustic beam enforced on the bow shock near the leading edge, and a blowing-suction slot on the wedge surface. They concluded that these three types of forcing eventually resulted in the same type of instability waves in the boundary layer. However the receptivity mechanism was not studied in detail. Ma and Zhong [16] studied the receptivity mechanisms of the same hypersonic boundary layer to various freestream disturbances, i.e., fast and slow acoustic waves, vorticity waves, and entropy waves, by solving the two-dimensional compressible Navier-Stokes equations. They found that the stable

7

modes in the boundary layer played a very important role in the receptivity process.

In this project, the receptivity mechanism of the Mach 8 flow over the sharp wedge to wall blowing-suction is investigated in detail by series of numerical simulations. The steady base flow is simulated by solving the two-dimensional compressible Navier-Stokes equations with a combination of a fifth-order shock-fitting finite difference method and a second-order TVD scheme. In the receptivity simulations, periodic blowing-suction disturbances are introduced to the steady base flow through a forcing actuator on the wedge surface. The characteristics of boundary-layer wave modes are identified and evaluated by comparing the results of LST and numerical simulations. The effects of frequency and location of the forcing actuator on the receptivity process are studied by considering seven cases of different blowing-suction locations with 15 frequencies for each case. Furthermore, the effects of profile and length of the forcing actuator are investigated. For all cases considered in this paper, forcing waves are weak enough so that the disturbances in the boundary layer are linear. The contours of the instantaneous pressure perturbation induced by blowing-suction disturbance are shown in Fig. 3. After the blowing-suction slot, the excited pressure perturbations are divided into two branches: one branch penetrates the boundary layer and propagates along the Mach lines (acoustic waves) while the other branch stays within the boundary layer, which is the unstable mode (mode S), indicated by the typical wave structures near the wall. The amplification of instantaneous pressure perturbation along the wedge surface also indicates the excitation of mode S.
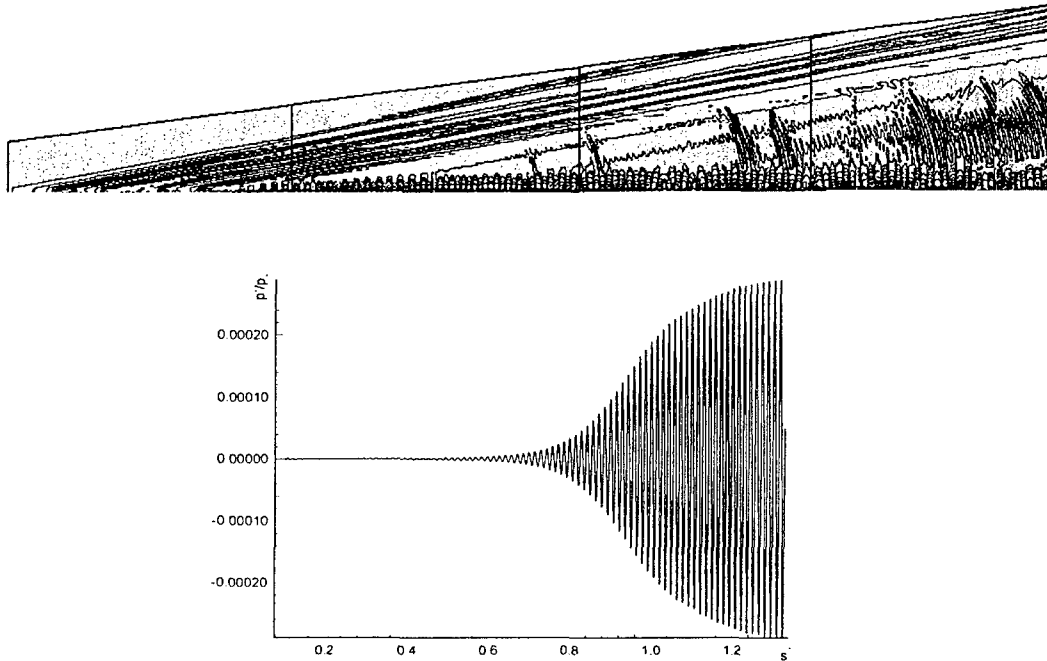

Fig. 3 Numerical simulation of receptivity of the Mach 8 flow over a sharp wedge to wall blowing-suction: 1) instantaneous pressure perturbation field; 2) instantaneous pressure perturbation along the surface.

The numerical results show that mode F, mode S, and acoustic modes are simultaneously excited by

8

wall blowing-suction disturbances. Downstream of the forcing region, mode F decays owing to its inherent stability whereas mode S grows because of its instability. Acoustic modes radiate into the external flow outside the boundary layer. As a result, mode S eventually becomes the dominant wave mode in the boundary layer. It is found that the frequency of the blowing-suction actuator has a significant effect on the receptivity process owing to the frequency dependence of the synchronization point between mode F and mode S. The numerical results also show that the excitation of mode S is strongly affected by profile and length of the forcing actuator. All cases of numerical simulations consistently show that the synchronization point plays an important role in the excitation of mode S by wall blowing-suction, i.e., mode S is strongly excited only when the blowing-suction actuator is located upstream of the synchronization point. When the forcing actuator is downstream of the synchronization point, there is very little excitation of mode S, despite the fact that the blowing-suction actuator is still located within the unstable region of mode S.

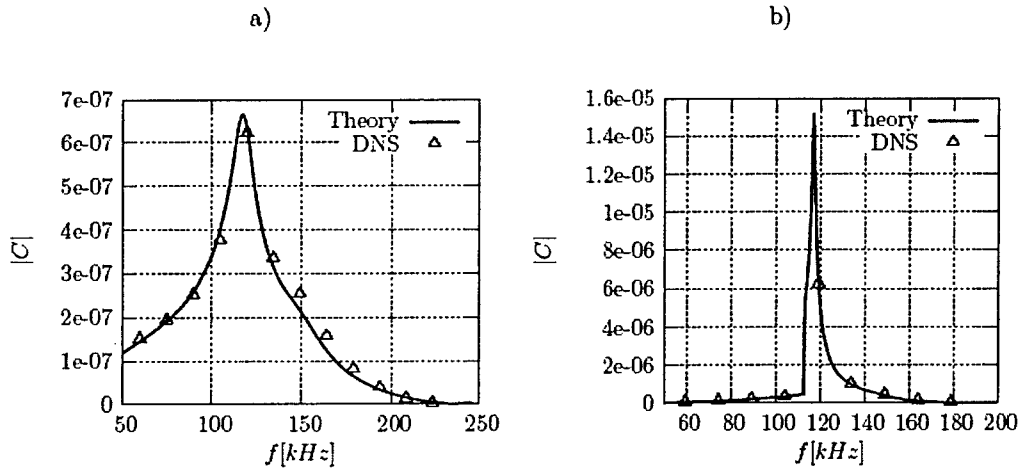a)   b)

Fig. 4 Comparison of the theoretical prediction for the receptivity coefficient with data filtered out from the computational results for receptivity of a hypersonic boundary layer to wall blowing-suction: a) mode S and b) mode F.

On the other hand, numerical simulation results require careful analytical analysis in order to gain a deeper understanding of the underlining physics in high-speed boundary-layer transition. A close collaboration between numerical and theoretical study of the receptivity phenomena will not only verify both sets of results, but also lead to better understanding of flow physics. We have started working in this direction with Professor Tumin [2, 17] in University of Arizona. Specifically, direct numerical simulation of receptivity in a boundary layer over a sharp wedge of half-angle 5.3° was carried out with two-dimensional perturbations introduced into the flow by periodic-in-time blowing-suction through a slot. The free-stream Mach number was equal to 8. The perturbation flow-field downstream from the slot was decomposed into normal modes with the help of the biorthogonal eigenfunction system. Filtered-out amplitudes of two discrete normal modes and of the fast acoustic modes are compared with the linear receptivity problem solution. Fig. 4 shows a comparison of the theoretical receptivity coefficient with the amplitude filtered out from the computational results by the theoretical analysis. One can see from the figure that there is an

excellent agreement between amplitudes calculated with the help of the theoretical receptivity model.

3.3 Receptivity to various two-dimensional wall perturbations of a Mach 5.92 flat-plate boundary layer flow

Publications: [10], [13]

The receptivity of a Mach 5.92 boundary-layer flow over a flat plate to periodic two-dimensional wall perturbations is investigated by numerical simulations and linear stability theory (LST). The flow conditions are the same as those of Maslov et al.'s leading-edge experiment [10]. The steady base flow is simulated by solving two-dimensional compressible Navier-Stokes equations with a combination of a fifth-order shock-fitting method and a second-order TVD scheme. Accuracy of the numerical steady base flow is validated by comparing with the theoretical self-similar boundary-layer solution and the published experimental results. The characteristics of boundary-layer wave modes are identified and evaluated by comparing the results of LST and numerical simulations. In receptivity simulations, three types of periodic two-dimensional wall perturbations, oscillation, blowing-suction, and temperature perturbation, are considered. All wall perturbations are introduced to the steady base flow by a forcing slot located on the flat plate. Effects of the perturbation type and the profile of temperature perturbation on receptivity process are studied by considering six cases of wall perturbations. Fig. 5 compare normalized Mach number and dimensionless streamwise velocity distributions across the boundary layer at three different locations of x* = 96 mm, 121 mm, and 138 mm. The numerical results agree well with the experimental results and the boundary-layer solution near the plate. However, in the region of η > 5, the numerical results have a better agreement with the experimental results. The difference between the numerical results and the boundary-layer solution is mainly caused by the existence of the bow shock, because the effect of the bow shock is neglected in the calculation of the compressible boundary-layer equations.
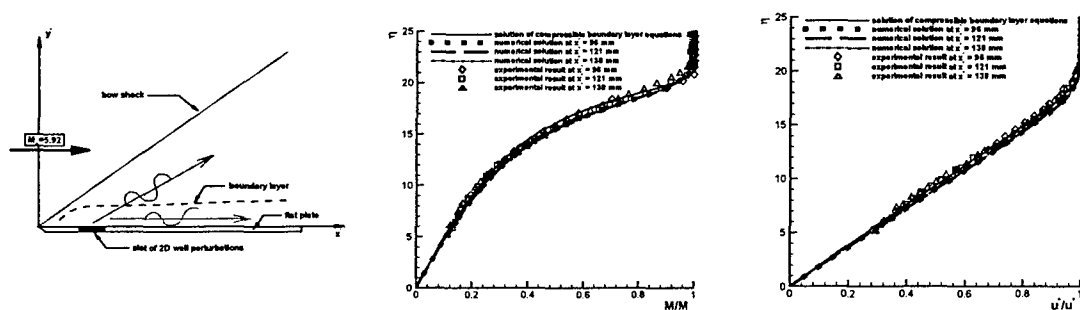

Fig. 5 Numerical simulation of a Mach 5.92 flat-plate boundary layer to two-dimensional wall perturbations and comparisons of normalized Mach number and dimensionless streamwise velocity.
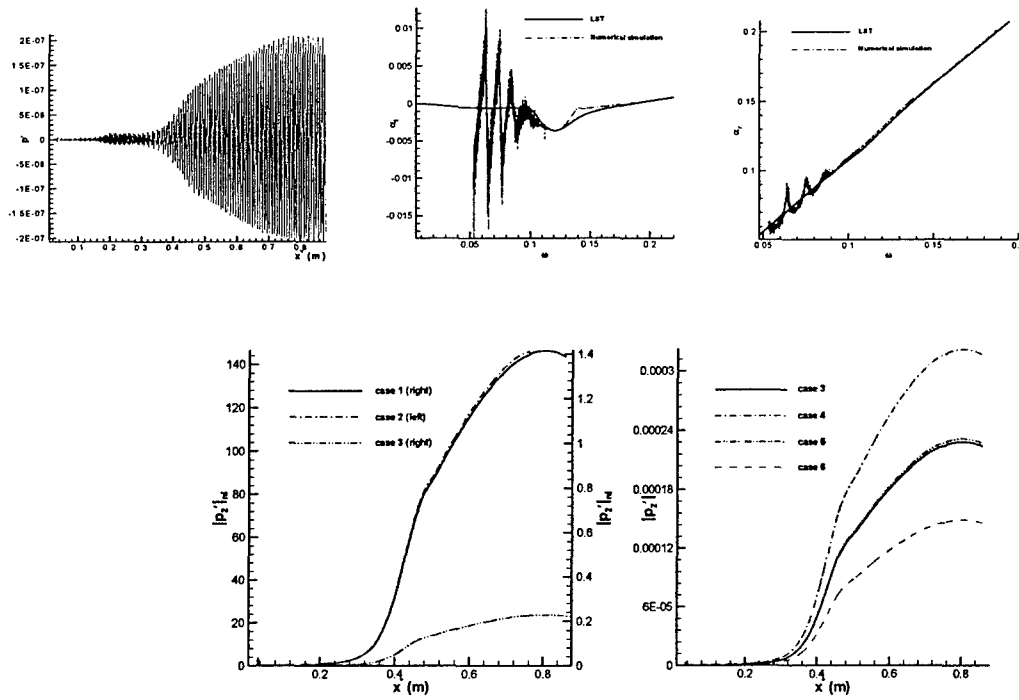
Fig. 6 Numerical simulation of receptivity of the Mach 5.92 flow over a flat plate to two-dimensional wall perturbations: 1) instantaneous pressure perturbation along the wall; 2) comparison of numerical and LST growth rates; 3) comparison of numerical and LST wave number; 4) amplitude comparison of pressure perturbation (100 kHz) for cases of wall oscillation, blowing-suction, and temperature perturbation; 5) amplitude comparison of pressure perturbation (100 kHz) for temperature perturbations of different profile.

Fig. 6 shows that all six cases of two-dimensional wall perturbations eventually result in the same type of instability wave (mode S) in the boundary layer. The hypersonic boundary-layer flow is most sensitive to wall blowing-suction and least sensitive to wall temperature perturbation. It is noticed that the profile of temperature perturbation has a strong effect on receptivity process. The receptivity of the hypersonic boundary layer to temperature perturbation is proportional to the energy introduced to the steady base flow, where the energy is determined by the profile of temperature perturbation.

3.4 Roughness induced transient growth in a Mach 7.99 flow over a blunt cone and the Mach 5.92 flat-plate boundary layer

Publications: [10], [11], [15]

Recent theoretical studies have shown the importance of transient growth and surface roughness in bypass transition [18, 19]. Reshotko and Tumin [20] have developed a model for roughness induced transient-growth transition. So far, there has not been any direct numerical simulation study on transient growth in hypersonic boundary layers. Furthermore, it is not known how the optimal disturbances computed by the transient growth theory are generated by surface roughness. These are

11

important issues related to the receptivity of transient growth. We use direct numerical simulation to conduct such studies because the complete receptivity process and transient growth can be simulated with minimum simplification assumptions. In the review period, we have done simulation studies on roughness induced transient growth for hypersonic flow over blunt bodies and a flat plate. The basic approach is to impose stationary 3-D surface roughness in the early stable region of the steady base hypersonic boundary layers. The subsequent development of disturbances in the boundary layer is captured by numerical simulations.
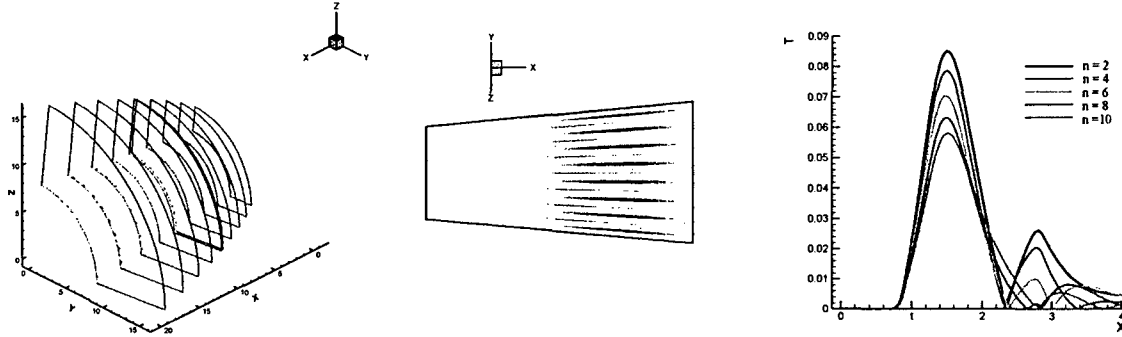

Fig. 7 Simulation solutions of temperature perturbations due to distributed surface roughness for Case D of Mach 7.99 flow over a blunt cone with 88.9 mm nose radius.

The specific flow conditions for the blunt cones are the same as Stetson's Mach 7.99 flow over a 7 deg. half angle blunt cones with the four sets of nose radii (Cases A to D). So far, only small distributed surface roughness has been imposed on the surface in the following form: $h(s,\theta) = \varepsilon h_0 (\sum_n A_n \cos(2\pi n\theta + \varphi_n)) f(s)$. Fig. 7 shows the results of temperature perturbations for Case D with nose radius of 88.9 mm. The flow perturbation induced by weak surface roughness shows the growth of disturbances along the cone surface. Work is currently under way to extend these initial studies to longer computational domain and to study the transient growth properties induced by surface roughness.
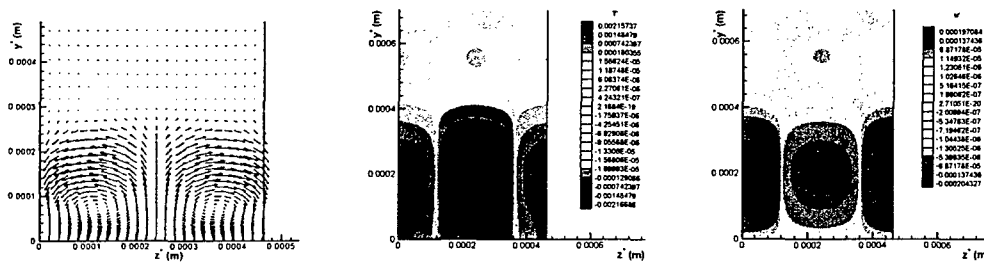
Fig. 8. Numerical simulation of receptivity of the Mach 5.92 flow over a flat plate to three-dimensional stationary roughness element: 1) vector plot of wall-normal and spanwise velocity perturbations in the wake region; 2) contours of temperature perturbation in the wake region; 3) contours of streamwise velocity perturbation in the wake region.

We have also studied the receptivity to three-dimensional stationary roughness elements of a

hypersonic flat-plate boundary layer, corresponding to Maslov et al.'s leading-edge experiment [10]. The surface roughness is periodic in spanwise direction. Effect of thermal flat plate boundary conditions on the receptivity process is considered by comparing numerical simulations on adiabatic and isothermal flat plates, respectively. Fig. 8 shows that counter rotating streamwise vortices are excited by stationary roughness element. The temperature increases in the wake region of roughness peak whereas it decreases in the wake region of roughness valley. Furthermore, the speed of wake from roughness peak is slower than that from roughness valley. It is also concluded based on the numerical results that the roughness element on adiabatic flat plate is more efficient in the excitations of streamwise vortices and transient growth.

3.5 Development of a new high-order immersed interface method

Publications: [2], [12]

During three-year project, we developed a new high-order immersed interface method for computing boundary layer transition with surface roughness. The work was motivated by discussions among the participants in the Transition Study Group Open Forum Held in the AIAA meeting in Reno in January 2005. It was pointed out that that there is a need to compute boundary layer stability and transient growth with distributive surface roughness. The methods for simulating flow with irregular surface are similar to those for simulation of multi-phase flows or fluid-structure interaction. A major difficulty in such simulation is due to the fact that the flow variables and their derivatives are not continuous across the interface or irregular surface. One way to simulate surface roughness of an arbitrary shape is to use the immersed boundary method [21] or the immersed interface method (IIM) of Laveque and Li [22] with a fixed, non-body fitted grid. The main drawback of the immersed boundary method is the fact that it is at most first order accurate at the interface. The immersed interface method can achieve a second order accuracy. But the IIM method is difficult to be used in complex flow problems. In order to maintain a second order accuracy, it is necessary to know the jump conditions of flow variables and the jump conditions for the first and the second derivatives at the interface.

For a uniformly high-order simulation of flow with surface roughness, we have developed a new high-order IIM method [11]. The new method can be arbitrarily high-order accuracy in the whole flow field, including the interface with discontinuity. So far, the new uniformly 2nd and 4th order accurate IIM methods have been tested for a number of 1-D and 2-D model equations with discontinuous interfaces. Figure 5 shows the result of a 2-D example used by Leveque and Li [22]

for the following elliptical equation, $\dfrac{d^2u}{dx^2} + \dfrac{d^2u}{dy^2} = \int_\Gamma 2\delta(x - X(s))\delta(y - Y(s))ds$, where the interface

is a circle of radius 0.5 centered at the origin. There is a jump for the normal velocity gradient at the interface. A uniform grid of N points is used in the numerical computations. The results are compared for three different numerical methods: (1) our IIM method A: 2nd order accuracy in both regular and interface grids, (2) our IIM method B: 4th order accuracy in regular grids and 3rd order in irregular grid points, and (3) Leveque and Li's 2nd order IIM [22]. Fig. 9 shows that the new IIM

method captures the interface accurately. Table 1 shows that the new 4th order IIM method is most accurate among these three methods. The results of this test case and other test cases show the potential of the new high-order IIM method in accurately computing flow with irregular surface, as well as two-phase flow problems. We plan to apply the new methods to the simulation of boundary layer transient growth with distributed surface roughness.

Table 1. <u>Comparison of Numerical Solutions of Three Methods</u>

	Leveque and Li's IIM method (2nd order) [4]	Current IIM method A (2nd order)	Current IIM method B (4th order)
Errors (80 by 80 grid)	2.45×10^{-4}	6.70×10^{-5}	2.31×10^{-6}
Error Ratios	3.41	3.90	12.6
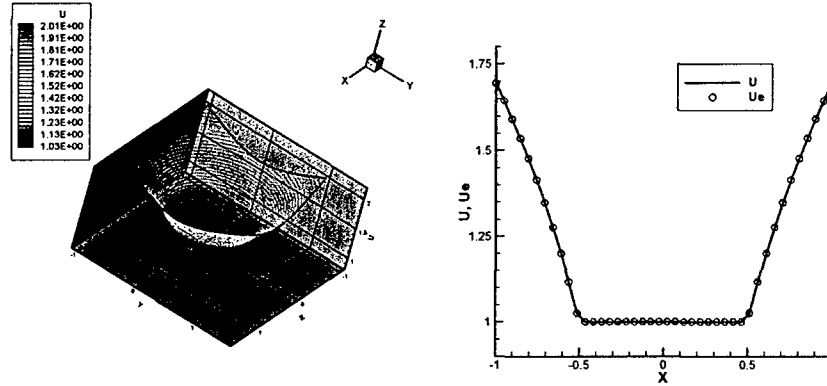
Fig. 9 Solution contours with discontinuous gradient at the interface and comparison of exact solution with the new 2nd order IIM method A for computing the 2-D model equation with a singular source term.

3.6 Stability and receptivity of hypersonic flow over the FRESH areoshell

At the request of Dr. John Schmisseur, we worked with Drs. Datta Gaitonde and Roger Kimmel of AFRL on a computational study of the stability and receptivity of the FRESH aeroshell. One of the objectives of the FRESH is to measure smooth-body and roughness-induced transition on the cone surface. The aeroshell has a spherical cone with a 7 degree half angle. It uses either a sharp nose or a slightly blunt nose. The objectives of our DNS studies are to compare our results with other simulation results obtained by AFRL and to do DNS studies of the stability and receptivity of hypersonic boundary layers over the aeroshell. So far, we have finished the computations of the mean flow of a test case with the same conditions as a wind tunnel test of the model. The flow conditions (air) are: $M_\infty = 6.5$, $T_\infty = 225.56K$, $\rho_\infty = 1.44 \times 10^{-1} kg/m^3$, $r_n = 2.5mm$, the cone half angle is 7 degrees, $T_w = 300K$ (isothermal wall), $Re_\infty = 19.1 \times 10^6 m^{-1}$, the first part of the model

14

without the flare is 1.0 meter long. Fig. 10 shows our steady flow solutions computed by the fifth-order shock fitting code. The outer computational boundary is the bow shock obtained by the simulation. The figure shows a very good resolution of the flow field.
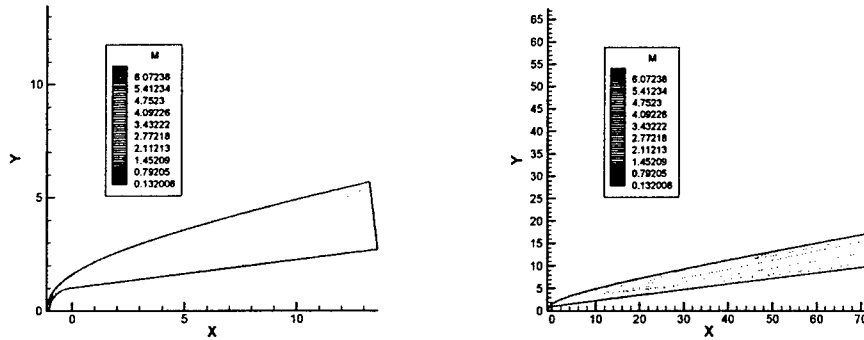

Fig. 10 Steady flow Mach number contours for the FRESH model with Mach 6.5 over a 7 deg. half angle blunt cone. The coordinates are non-dimensionalized by the cone nose radius of 2.5 mm.

4 SUMMARY OF RESEARCH ACCOMPLISHMENTS

In the report period, we have mainly focused on the DNS studies of receptivity of supersonic and hypersonic boundary layer flows. DNS results are compared with Maslov's leading-edge receptivity experiment on Mach 5.92 flow over a flat plate, and Stetson's 1984 stability experiment on Mach 7.99 flow over a blunt cone. We also collaborate with Prof. Tumin in University of Arizona to compare numerical and theoretical results on receptivity of a Mach 8 flow over a sharp wedge to wall blowing-suction, and to deeply analyze the receptivity characteristics. Our numerical studies have been validated to be of high accuracy and led to further understanding of hypersonic boundary layer receptivity mechanisms. The main research accomplishments are

1. We have conducted DNS studies on the receptivity of a Mach 8.0 flow over a sharp wedge of a half-angle of 5.3° to wall blowing-suction. The results show that Mode F, mode S, and acoustic modes are simultaneously excited by wall blowing-suction disturbances. Downstream of the forcing region, mode F decays owing to its inherent stability whereas mode S grows because of its instability. Acoustic modes radiate into the external flow outside the boundary layer. As a result, mode S eventually becomes the dominant wave mode in the boundary layer. It is also found that the frequency of the blowing-suction actuator has a significant effect on the receptivity process owing to the frequency dependence of the synchronization point between mode F and mode S. Furthermore, the excitation of mode S is strongly affected by profile and length of the forcing actuator. All cases of numerical simulations consistently show that the synchronization point plays an important role in the excitation of mode S by wall blowing-suction, i.e., mode S is strongly excited only when the blowing-suction actuator is located upstream of the synchronization point. When the forcing actuator is downstream of the

15

synchronization point, there is very little excitation of mode S, despite the fact that the blowing-suction actuator is still located within the unstable region of mode S.

2. We collaborated with Prof. Tumin in University of Arizona to compare numerical and theoretical results on receptivity of the Mach 8 flow over a sharp wedge to wall blowing-suction, and to deeply analyze the receptivity characteristics. The perturbation flow field downstream of the blowing-suction actuator was decomposed into boundary-layer wave modes with the help of the biorthogonal eigenfunction system. It was shown that amplitudes of boundary-layer wave modes calculated with the help of the theoretical receptivity model had good agreements with those obtained by projecting the numerical results onto the boundary-layer wave modes

3. We have studied the receptivity of a Mach 5.92 over a flat plate to various two-dimensional wall perturbations: oscillation, blowing-suction, and temperature perturbation. The numerical results show that all types of two-dimensional wall perturbations eventually result in the same type of instability wave (mode S) in the boundary layer. The hypersonic boundary-layer flow is most sensitive to wall blowing-suction and least sensitive to wall temperature perturbation. It is also noticed that the profile of temperature perturbation has a strong effect on receptivity process. The receptivity of the hypersonic boundary layer to temperature perturbation is proportional to the energy introduced to the steady base flow, where the energy is determined by the profile of temperature perturbation.

4. We have conducted DNS studies on the transient growth phenomena of a Mach 5.92 flat-plate boundary layer and a Mach 7.99 flow over a blunt cone to small-scale three-dimensional stationary roughness element. The surface roughness is periodic in spanwise direction. Effect of thermal flat plate boundary conditions on the receptivity process is considered by comparing numerical simulations on adiabatic and isothermal flat plates, respectively. The numerical results show that counter rotating streamwise vortices are excited by stationary roughness element. The temperature increases in the wake region of roughness peak whereas it decreases in the wake region of roughness valley. Furthermore, the speed of wake from roughness peak is slower than that from roughness valley. All these results are consistent with those of Tumin's theoretical analysis. It is also concluded based on the numerical results that the roughness element on adiabatic flat plate is more efficient in the excitations of streamwise vortices and transient growth.

5. We developed a new high-order immersed interface method for computing boundary layer transition with surface roughness. The work was motivated by discussions among the participants in the Transition Study Group Open Forum Held in the AIAA meeting in Reno in January 2005. It was pointed out that that there is a need to compute boundary layer stability and transient growth with distributive surface roughness. The new method can be arbitrarily high-order accuracy in the whole flow field, including the interface with discontinuity, and it can be useful for the simulations of transient growth to finite or nonlinear surface roughness.

5   RESULTS OF HYPERSONIC BOUNDARY LAYER RECEPTIVITY

One of the major accomplishments of the current research project is on revealing the receptivity mechanism of a hypersonic boundary layer to wall blowing-suction, and the effect of blowing-suction locations of forcing regions. These results are discussed in more detail in this section. Details of these results have been published in **Publications: [2], [6], [13], [15], [20].**

5.1 Flow conditions and blowing-suction model

With the development of advanced computers and numerical techniques, numerical simulation of the receptivity process by directly solving Navier-Stokes equations has become feasible. By solving the compressible linearized Navier-Stokes equations, Malik et al. [15] investigated the responses of a Mach 8 flow over a sharp wedge of a half-angle of $5.3°$ to three types of external forcing: a planar free-stream acoustic wave, a narrow acoustic beam enforced on the bow shock near the leading edge, and a blowing-suction slot on the wedge surface. They concluded that these three types of forcing eventually resulted in the same type of instability waves in the boundary layer. However the receptivity mechanism was not studied in detail. Ma and Zhong [16] studied the receptivity mechanisms of the same hypersonic boundary layer to various freestream disturbances, i.e., fast and slow acoustic waves, vorticity waves, and entropy waves, by solving the two-dimensional compressible Navier-Stokes equations. They found that the stable modes in the boundary layer played a very important role in the receptivity process.
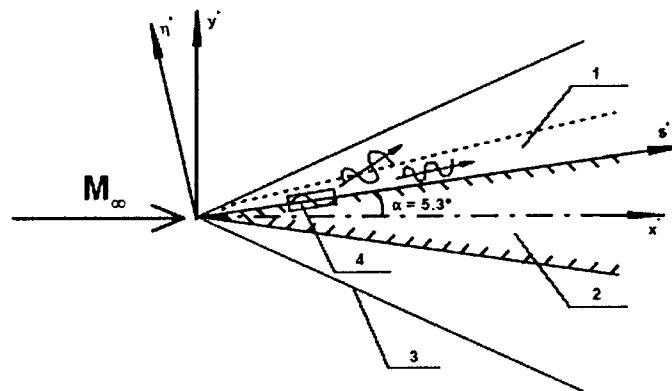
Fig. 11 A schematic of the receptivity of a hypersonic boundary layer over a sharp wedge to wall blowing-suction: 1. boundary layer; 2. sharp wedge; 3. bow shock; 4. blowing-suction actuator.

In this project, the receptivity mechanism of the Mach 8 flow over the sharp wedge to wall blowing-suction is investigated by series of numerical simulations. Fig. 11 shows a schematic of the receptivity of a hypersonic boundary layer over a sharp wedge to wall blowing-suction. Due to the symmetric geometry, only the flow field over the upper surface of the sharp wedge is simulated. The steady base flow is simulated by solving the two-dimensional compressible Navier-Stokes equations with a combination of a fifth-order shock-fitting finite difference method and a

second-order TVD scheme. In the receptivity simulations, periodic blowing-suction disturbances are introduced to the steady base flow through a forcing actuator on the wedge surface. The characteristics of boundary-layer wave modes are identified and evaluated by comparing the results of LST and numerical simulations. The effects of frequency and location of the forcing actuator on the receptivity process are studied by considering seven cases of different blowing-suction locations with 15 frequencies for each case.

The freestream conditions for the currently studied hypersonic flow over the sharp wedge are the same as those used by Malik et al. [15], and Ma and Zhong [16], i.e.,

$$M_{\infty} = 8.0, \qquad\qquad T_{\infty}^* = 54.78\,\text{K}$$

$$p_{\infty}^* = 389\,\text{Pa}, \qquad\qquad P_r = 0.72$$

$$\text{Re}_{\infty} = \rho_{\infty}^* u_{\infty}^* / \mu_{\infty}^* = 8.2 \times 10^6\,\text{m}^{-1}$$

Total length of the wedge surface $\approx 1.5\,\text{m}$

For the simulation of steady base flow, the wall is adiabatic, and the physical boundary condition of velocity on the wedge surface is the non-slip condition. When periodic blowing-suction disturbances are enforced on the steady base flow, the isothermal temperature condition is applied on the wall. This temperature condition is a standard boundary condition for theoretical and numerical studies of high frequency disturbances. Meanwhile, non-slip condition is applied on the wall except the forcing region. Inlet conditions are specified. High-order extrapolation is used for outlet conditions because the flow is supersonic at the exit boundary except a small region near the wedge surface.

In Fedorov and Khokhlov's [23] theoretical and numerical analysis of boundary-layer receptivity to wall disturbances, wall blowing-suction disturbance has the following traveling-wave form:

$$\begin{bmatrix} u' \\ v' \\ w' \\ \theta' \end{bmatrix} = g(x) \begin{bmatrix} 0 \\ 1 \\ 0 \\ 0 \end{bmatrix} e^{(i\alpha_c x + i\beta_c z - i\omega t)} \tag{1}$$

where u', v', w' are velocity disturbances in streamwise, wall-normal, and spanwise directions, respectively, while θ' is the temperature disturbance. The parameters α_c and β_c are wave number components in streamwise and spanwise directions, and ω is the circular frequency. The function $g(x)$ represents the disturbance profile. Equation (1) implies that wall blowing-suction is only related to the wall-normal velocity disturbance. For this model, small instantaneous mass flux is generally introduced to the boundary layer.

Another model of blowing-suction disturbances is to enforce the mass flux oscillations on the wall, which has been used by Eibler and Bestek [24], and Egorov et al. [25]. For this model, wall blowing-suction is expressed as

$$\frac{\rho_w v_w}{\rho_\infty u_\infty} = q_w(x,t) = A\sin\left(2\pi\frac{x-x_1}{x_2-x_1}\right)\sin\omega t \qquad (2)$$

where A is the amplitude of mass flux oscillation, ρ_w and v_w are the local density and wall-normal velocity at the location x on the wall, ρ_∞ and u_∞ are the density and stream-wise velocity in free-stream. The coordinates x_1 and x_2 represent the leading and trailing edges of the blowing-suction actuator. Due to the anti-symmetric profile of sine function within the forcing region, the net mass flux introduced to the boundary layer is zero at any instant.

In current study, a blowing-suction model similar to Eq. (2) is used. The mass flux oscillations on the wedge surface within the blowing-suction region can be written as:

$$\left(\rho^* v^*\right)' = q_0^* \varepsilon \beta(l) \sum_{n=1}^{15} \sin\omega_n^* t^* \qquad (3)$$

where q_0^* is a local constant depending on the location of the blowing-suction actuator, and ε is a small dimensionless parameter representing the amplitude of the mass flux oscillation. The function $\beta(l)$ is the profile function defined within the forcing region as

$$\beta(l) = \begin{cases} 20.25l^5 - 35.4375l^4 + 15.1875l^2 & \text{if} \quad l \le 1 \\ -20.25(2-l)^5 + 35.4375(2-l)^4 - 15.1875(2-l)^2 & \text{if} \quad l \ge 1 \end{cases} \qquad (4)$$

The variable l is a dimensionless coordinate defined within the blowing-suction region,

$$l = \frac{2(s^* - s_i^*)}{s_e^* - s_i^*} \qquad (5)$$

where s_i^*, s_e^* are the coordinates of the leading and trailing edges of the blowing-suction actuator.

Compared with the sine profile function in Eq. (2), the specific 5th-order-polynomial profile function makes smoother the mass flux oscillations at the edges of the forcing actuator. Due to the anti-symmetric property of the 5th-order-polynomial profile function within the blowing-suction region, the net mass flux introduced to the boundary layer is zero at any instant. In Eq. (3), ω_n^* is the circular frequency of multi-frequency blowing-suction disturbances $(n=1,2,\cdots,15)$, which is related to the frequency by,

$$\omega_n^* = 2\pi f^* = 2n\pi f_1^* \quad (n=1,2,\cdots,15) \qquad (6)$$

19

The circular frequency, ω_n^*, and the frequency, f_n^*, are non-dimensionalized according to

$$\omega_n = \frac{\omega_n^* L^*}{u_\infty^*}, L^* = \sqrt{\frac{\mu_\infty^* s^*}{\rho_\infty^* u_\infty^*}} \tag{7}$$

$$F_n = \frac{2\pi f_n^* \mu_\infty^*}{\rho_\infty^* u_\infty^{*2}} = \frac{\omega_n^* \mu_\infty^*}{\rho_\infty^* u_\infty^{*2}} \tag{8}$$

The current receptivity studies are focused on linear responses of the boundary layer to forcing waves. In the simulations, the amplitude of mass flux oscillation is small enough to preserve the linear properties of the disturbances. The dimensionless amplitude coefficient, ε in Eq. (3), is given as

$$\varepsilon = 1.0 \times 10^{-5} \tag{9}$$

5.2 Steady base flow

The steady base flow is simulated by solving the two-dimensional compressible Navier-Stokes equations with a combination of a fifth-order shock-fitting finite difference method and a second-order TVD scheme. In the leading edge region, there exists a singular point at the tip of the wedge, which will introduce numerical instability if the fifth-order shock-fitting method is used to simulate the flow. Therefore, the computational domain for the fifth-order shock-fitting method starts at $s^* = 0.00409\,\text{m}$ and ends at $s^* = 1.48784\,\text{m}$, respectively. In actual simulations, the computational domain is divided into **30** zones with a total of **5936** grid points in stream-wise direction and **121** grid points in wall-normal direction. Forty-one points are used in the overlap region between two neighboring zones, which is proved to be sufficient to make the solution accurate and smooth within the whole domain. An exponential stretching function is used in the wall-normal direction to cluster more points inside the boundary layer. On the other hand, the grid points are uniformly distributed in stream-wise direction. The spatial convergence of the results based on this grid structure has been evaluated by grid refinement studies to ensure the grid independence of the numerical simulations. The results of the evaluation of numerical accuracy can be found in Ma and Zhong's paper [16], they are not repeated here.

For the first zone of the shock-fitting calculations, the inlet conditions are obtained from the results of the second-order TVD shock-capturing scheme which is used to simulate the steady base flow in a small region including the leading edge. For other zones, inlet conditions are interpolated from the results of the previous zone. Fig. 12 shows the wall-normal velocity and density contours near the leading edge of the steady base flow obtained by the second-order TVD scheme and the fifth-order shock-fitting method. The flow field including the leading edge is simulated by the TVD scheme, whereas the flow field after $s^* = 0.00409\,\text{m}$ is simulated by the shock-fitting method. The region between $s^* = 0.00409\,\text{m}$ to $s^* = 0.0064\,\text{m}$ is an overlap region where the flow is computed by

20

both methods. This figure shows that wall-normal velocity and density contours have good agreements within the overlap region, which indicates that the TVD solutions are accurate to be used as inlet conditions for the fifth-order shock-fitting simulation in the first zone. The combination of the shock-fitting method and the TVD scheme has also been validated in simulations of supersonic and hypersonic steady base flows over a flat plate by Ma and Zhong [26], and Wang and Zhong [4].
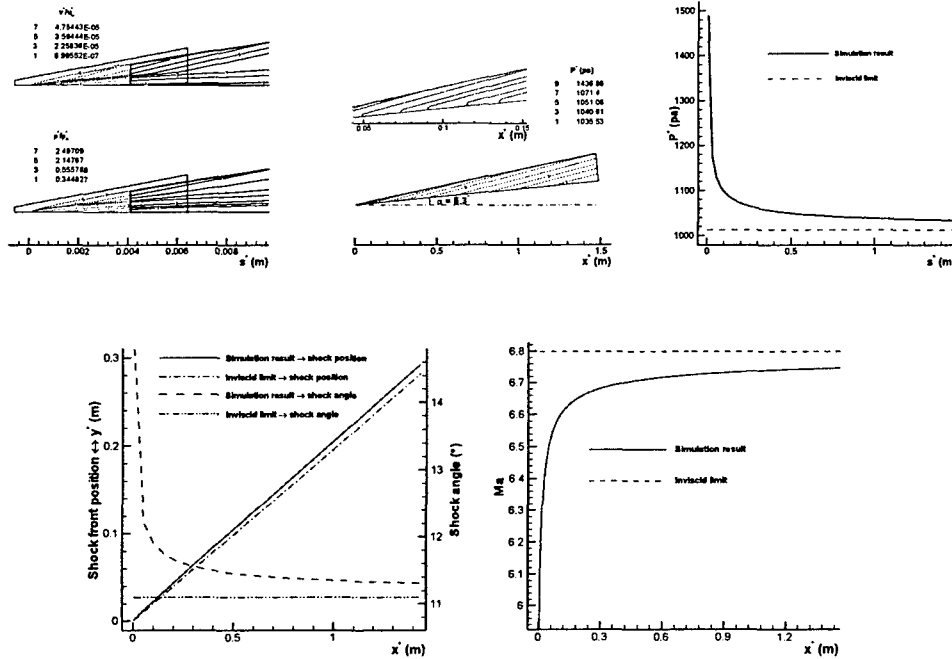

Fig. 12 Numerical results of steady base flow: 1) wall-normal velocity and density contours near the leading edge; 2) pressure contour; 3) pressure distributions along the wedge surface; 4) shock front position and distribution of the shock angle; 5) distribution of Mach number behind the bow shock.

Fig. 12 shows the pressure contours of the steady base flow simulated by the fifth-order shock-fitting finite difference method. The upper boundary of the flow field represents the bow shock induced by the sharp wedge and the displacement thickness of the boundary layer. The lower boundary is the surface of the sharp wedge of a half angle of $5.3°$. A part of the pressure field from

$x^* = 0.05$ m to $x^* = 0.15$ m is amplified to show clearly the pressure contour within the

boundary layer. It is noticed that pressure is approximately a constant across the boundary layer and along the Mach lines, which is consistent with the theories of the boundary layer flow and inviscid

supersonic aerodynamics. At a fixed location (constant x^*), pressure behind the shock is higher

than that on the wedge surface due to the existence of the bow shock. Fig. 12 also shows the pressure distribution along the wedge surface obtained by the fifth-order shock-fitting method. The theoretical inviscid limit is also plotted in the figure for comparison. Near the leading edge, there exists great pressure gradient for the numerical result, which is caused by the interaction between the inviscid outer flow and the viscous boundary layer. From upstream to downstream, the

21

outer-flow/boundary-layer interaction becomes weaker with the bow shock moving away from the boundary layer. As a result, the pressure approaches the constant value of the inviscid limit further downstream. The figure also shows that the pressure of numerical solution at the exit of computational domain is greater than that of the theoretical inviscid limit. This difference in pressure is a result of the induced boundary layer thickness on the wedge surface.

The shock front position and the shock angle obtained by the numerical simulations are plotted together with those of the theoretical inviscid limit in Fig. 12. The solid line represents the shock front whereas the dashdot line is a straight line representing the oblique shock induced by an inviscid flow passing the sharp wedge with the same free-stream conditions. The figure shows that the shock front of numerical solution is not a straight line. The angle of the bow shock decreases from $14.793°$ near the leading edge to $11.307°$ at the exit of the computational domain, however the inviscid limit of the shock angle is a constant of $11.102°$. Fig. 12 shows the distribution of Mach number behind the bow shock of the numerical result. The theoretical inviscid limit of Mach number behind the oblique shock is also plotted in the figure for comparison. It shows that Mach number increases from 5.911 near leading edge to 6.746 at the exit of the computational domain. For inviscid Mach 8 flow over the sharp wedge of a half-angle of $5.3°$, Mach number behind the shock is 6.798. Figure 6 shows that the shock angle and Mach number behind the shock approach corresponding values of the theoretical inviscid limit further downstream, where the interaction between the inviscid outer flow and the viscous boundary layer becomes weak. Again, large gradients of the shock angle and Mach number behind the shock near the leading edge are caused by the interaction between the inviscid outer flow and the viscous boundary layer.

5.3 Characteristics of boundary-layer wave modes

The characteristics of boundary-layer wave modes of the Mach 8 flow over the sharp wedge of a half-angle of $5.3°$ is studied by LST based on a multi-domain spectral method of Malik [27]. The LST code was written by Ma and Zhong [28]. The velocity, pressure, and temperature disturbances are represented by harmonic waves of the form

$$\begin{Bmatrix} \tilde{u} \\ \tilde{v} \\ \tilde{w} \\ \tilde{p} \\ \tilde{T} \end{Bmatrix} = \begin{Bmatrix} \hat{u}(y) \\ \hat{v}(y) \\ \hat{w}(y) \\ \hat{p}(y) \\ \hat{T}(y) \end{Bmatrix} e^{i(\alpha_c x + \beta_c z - \omega_c t)} \tag{10}$$

Similar to Eq. (1), the parameters α_c and β_c are wave number components in streamwise and spanwise directions, and ω_c is the circular frequency. For the current two-dimensional flow cases, $\beta_c = 0$. Substituting disturbances of Eq. (10) and the steady base flow into the compressible linearized Navier-Stokes equations, an ordinary-differential-equation system is achieved, i.e.,

$$\left(A\frac{d^2}{dy^2} + B\frac{d}{dy} + C \right)\phi = 0 \tag{11}$$

where ϕ is the disturbance vector defined by $\{\hat{u}, \hat{v}, \hat{p}, \hat{T}, \hat{w}\}^T$. The coefficient matrices A, B, and C were given in Malik's paper [27]. In spatial stability analysis, the two parameters, ω_c and β_c, are specified as real numbers. The streamwise wave number, α_c, is a complex number and solved as the eigenvalue of the ordinary-differential-equation system. The complex wave number α_c can be expressed as

$$\alpha_c = \alpha_r + i\alpha_i \tag{12}$$

where α_i is the local growth rate. A boundary-layer wave mode is unstable when $\alpha_i < 0$ whereas it is stable when $\alpha_i > 0$. The real part, α_r, is the local wave number which can be used to define the local phase velocity:

$$a = \frac{\omega_c}{\alpha_r} \tag{13}$$

Both the wave number and the phase velocity can be used to identify the boundary-layer wave mode.
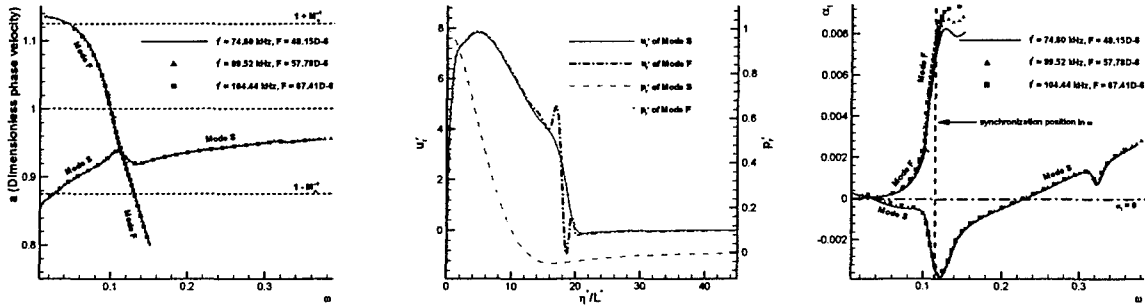
Fig. 13 Characteristics of boundary-layer modes: 1) distribution of dimensionless phase velocity; 2) eigenfunctions of boundary-layer mode at synchronization point; 3) distribution of growth rate.

Fig. 13 shows the dimensionless phase velocities of boundary-layer wave modes at three dimensionless frequencies as a function of the dimensionless circular frequency ω. These three frequencies are the same as F_5, F_6, and F_7 in Table 2. The three dashed lines represent the dimensionless phase velocities of fast acoustic mode ($a = 1 + M_\infty^{-1}$), vorticity or entropy mode ($a = 1$), and slow acoustic mode ($a = 1 - M_\infty^{-1}$), respectively. The excellent agreement of the phase

23

velocities at different dimensionless frequencies indicates that the phase velocity is a function of ω only. The figure clearly shows that mode F originates from fast acoustic mode. As ω increases, the phase velocity of mode F decreases and intersects that of vorticity or entropy mode. On the other hand, mode S originates from slow acoustic mode. The figure also shows that mode S synchronizes with mode F at the point of $\omega_s = 0.11443$ and $a_s = 0.93349$. At the synchronization point, the dimensionless phase velocities of mode S and mode F are the same, and their eigenfunctions have similar profile. The figure shows that the flow fluctuations are confined within the boundary layer. Except the differences near the edge of the boundary layer, the eigenfunctions of mode F and mode S agree very well at the synchronization point. Although Fig. 13 shows that the synchronization point at different frequencies have a constant value of $\omega_s (= 0.11443)$, the dimensional location of the synchronization point, s_{sn}^*, are different for different dimensionless frequencies. The synchronization location in s^* coordinate for a given dimensionless frequency can be calculated using the following formula

$$s_{sn}^* = \frac{\left(\omega_s/F_n\right)^2}{\text{Re}_\infty^*} \tag{14}$$

Fig. 13 also shows the growth rates of boundary-layer wave modes at the same set of three frequencies as a function of the dimensionless circular frequency. The vertical dashed line represents the position of the synchronization point, whereas the horizontal dashdot line stands for the neutral modes ($\alpha_i = 0$). The growth rates of either mode S or mode F of the three frequencies are almost the same, and they are approximately functions of ω only. Mode S is unstable in the region from $\omega_I = 0.04$ to $\omega_{II} = 0.23$ whereas mode F is always stable. For unstable mode S, it is also noticed that the growth rate upstream of the synchronization point ($\omega < 0.095$) is much larger than those around and downstream of the synchronization point. This indicates that mode S is more unstable around and downstream of the synchronization point. The parameters ω_I and ω_{II} are called the Branch I and Branch II neutral points of mode S. Mode S is stable upstream of Branch I neutral point and downstream of Branch II neutral point. The location of the Branch II neutral point in s^* coordinate, which changes with different dimensionless frequencies, can be calculated by

$$s_{IIn}^* = \frac{\left(\omega_{II}/F_n\right)^2}{\text{Re}_\infty^*} \tag{15}$$

Equations (14) and (15) show that when F increases, the corresponding s_{sn}^* and s_{IIn}^* decrease. In other words, the synchronization point and the Branch II neutral point move upstream when F increases. Table 2 lists dimensional frequency, dimensionless circular frequency, dimensionless

24

frequency, locations of synchronization point and Branch II neutral point for the 15 sets of frequencies considered in the current study

Table 2 **Dimensional frequency, dimensionless circular frequency, dimensionless frequency, locations of synchronization point and Branch II neutral point for the 15 sets of frequencies considered in the current study**

n	f_n^* (kHz)	ω_n^* (kHz)	$F_n \times 10^6$	s_{sn}^* (m)	s_{IIn}^* (m)
1	14.92	93.74	9.63	16.9885	68.38297
2	29.84	187.48	19.26	4.2471	17.09574
3	44.76	281.23	28.89	1.8876	7.59811
4	59.68	374.97	38.52	1.0618	4.27394
5	74.60	468.71	48.15	0.6795	2.73532
6	89.52	562.45	57.78	0.4719	1.89953
7	104.44	656.19	67.41	0.3467	1.39557
8	119.36	749.94	77.04	0.2654	1.06848
9	134.28	843.68	86.67	0.2097	0.84423
10	149.20	937.42	96.30	0.1699	0.68383
11	164.12	1031.16	105.93	0.1404	0.56515
12	179.04	1124.91	115.56	0.1180	0.47488
13	193.96	1218.65	125.19	0.1005	0.40463
14	208.88	1312.39	134.82	0.0867	0.34889
15	223.80	1406.13	144.45	0.0755	0.30392

5.4 Receptivity to a single-frequency blowing-suction actuator

The receptivity result of the hypersonic boundary layer to a blowing-suction actuator at a single frequency is firstly presented in this section. The forcing disturbance at the frequency of $f_s^* = 74.60$ kHz is introduced through a blowing-suction actuator on the wedge surface from $s_i^* = 0.10184$ m to $s_i^* = 0.11384$ m. Table 3 lists the parameters of the blowing-suction actuators at seven different locations. The dimensional values of q_0^* and other parameters of the forcing actuator considered in this section are the same as case 2 in Table 3. The value of ε is given in Eq. (9). Due to the fact that only very weak disturbances are considered, the current receptivity is in the linear region.

Fig. 14 shows the distribution of dimensionless instantaneous pressure perturbation along the wedge surface. The amplification of the pressure perturbation from upstream to downstream indicates the excitation of unstable modes in the boundary layer. The significant growth of the pressure

perturbation starts at a location close to the corresponding synchronization point at $s^*_{ss} = 0.6795$ m.

It is very likely that mode S is excited in the boundary layer by the blowing-suction disturbance, because mode S is more unstable around and downstream of the synchronization point.

Table 3 **Constant Error! Objects cannot be created from editing field codes. and other parameters of blowing-suction actuator for the seven cases by which the effect of location of the blowing-suction actuator on receptivity is investigated**

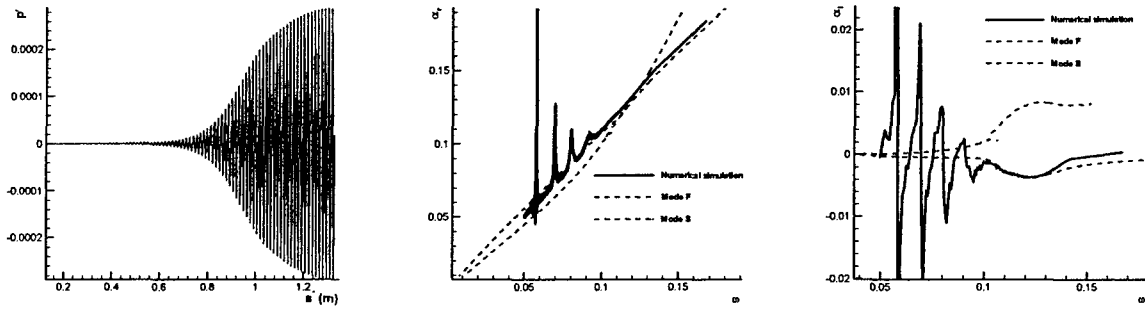| case	$q^*_0 (\text{kg/m}^2\text{s})$	s^*_i (m)	s^*_e (m)	s^*_c (m)
1	0.214139	0.05184	0.06384	0.05784
2	0.125188	0.10184	0.11384	0.10784
3	0.096130	0.15184	0.16384	0.15784
4	0.080666	0.20184	0.21384	0.20784
5	0.070759	0.25184	0.26384	0.25784
6	0.063745	0.30184	0.31384	0.30784
7	0.054453	0.40184	0.41384	0.40784

Fig. 14 Distribution of dimensionless pressure perturbation along the wedge surface and comparisons of numerical and LST local wave number and local growth rate.

In order to check the properties of the unstable modes, a Fourier transform is applied to the dimensionless instantaneous pressure perturbation along the wedge surface, which leads to

$$p'(s^*, t^*) = \sum |p'_n(s^*)| e^{i[\phi'_n(s^*) - \omega^*_n t^*]} \tag{16}$$

where $p'(s^*, t^*)$ represents the dimensionless instantaneous pressure perturbation along the wedge surface. In above equation, $|p'_n(s^*)|$ and $\phi'_n(s^*)$ are the perturbation amplitude and phase angle, respectively. Once $|p'_n(s^*)|$ and $\phi'_n(s^*)$ are known, a local wave number (α_{rn}) and a local growth rate (α_{in}) of the perturbation at the frequency f^*_n can be defined as

$$\alpha_{rn} = L^* \frac{d\phi'_n}{ds^*} \tag{17}$$

$$\alpha_{in} = -\frac{L^*}{|p'_n|} \frac{d|p'_n|}{ds^*} \tag{18}$$

where L^* is the length scale of local boundary layer thickness as defined by Eq. (7). The parameters α_{rn} and α_{in} will represent the true wave number and growth rate only if the disturbance is dominated by a single wave mode. Otherwise, the disurbance needs to be decomposed in order to check properties of a specific mode. For example, Tumin, Wang, and Zhong [2] decomposed the perturbation at a location just downstream of the blowing-suction actuator with a biorthogonal eigenfunction system, where mode F, mode S, and acoustic modes coexisted and none of them was dominant.

Since our focus is on numerical simulation results, we only consider the later stage where mode S is the dominant mode in the boundary layer. In this case, Eqs. (17) and (18) can be used to check the properties of the unstable mode S. Fig. 14 compares local wave numbers and local growth rates at the frequency f_s^* obtained by Eqs. (17) and (18) with the corresponding values of mode F and mode S computed by LST, respectively. These two figures show that wave numbers and growth rates of the numerical results agree well with those of mode S after the location of $\omega = 0.095$ ($s^* = 0.477$ m). As shown in Fig. 13, this is the location where the growth rate of mode S decrease significantly and mode S grows to the dominant mode in the boundary layer, which indicates that the unstable mode excited by the blowing-suction forcing is mode S. It is also shown that the two sets of growth rates agree very well for ω from **0.102** to **0.131**. When ω is larger than **0.131**, the growth rate from numerical simulation is larger than that from LST, which means that mode S obtained by numerical simulation becomes more stable than that predicted by LST. In other words, the Branch II neutral point of mode S obtained by numerical simulation moves upstream compared with that predicted by LST. A possible reason is due to the non-parallel effects that are not considered in linear stability theory. This result is consistent for all cases considered in the current study.

Fig. 15 compares the eigenfunctions of mode F and mode S with the amplitude of pressure perturbation obtained from the numerical simulation at four different locations. Figure (a) shows that the numerical pressure perturbation is not confined within the boundary layer, and it is quite different from the eigenfunctions of mode F and mode S. These characteristics of pressure perturbation are caused by the coexistence of mode F, mode S, and acoustic modes in the boundary layer just downstream of the blowing-suction region. Figure (b) shows that the numerical pressure perturbation is much closer to the eigenfunction of mode S, and it is almost confined within the boundary layer. These characteristics of pressure perturbation indicate that mode S becomes the dominant mode in the local boundary layer with acoustic modes radiating into the external flow outside the boundary layer and mode F decaying owing to its inherent stability. Figures (c) and (d)

27

show good agreements between the eigenfunctions of mode S and the pressure perturbation obtained from the numerical simulation, because mode S is the dominant mode in the local boundary layer downstream of $s^* \approx 0.6$ m.
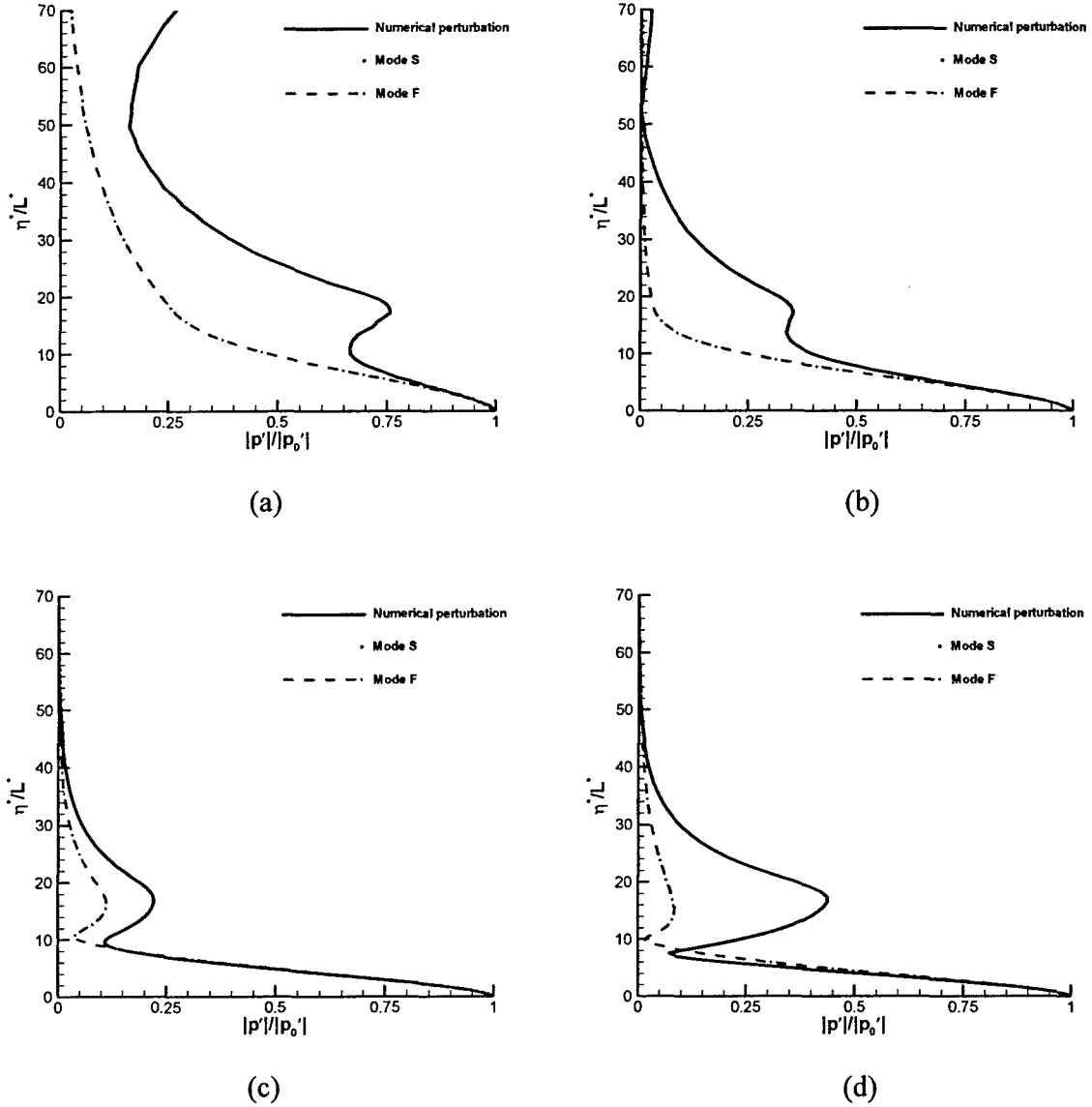

Fig. 15 Comparisons of the eigenfunctions of mode F and mode S with the amplitude of pressure perturbation obtained from numerical simulation at different locations: (a) $\omega=0.070872$ ($s^*=0.26534$ m); (b) $\omega=0.093855$ ($s^*=0.46534$ m); (c) $\omega=0.11223$ ($s^*=0.66534$ m); (d) $\omega=0.14530$ ($s^*=1.11534$ m).

The numerical results and analysis above show that mode F, mode S, and acoustic modes are simultaneously excited by the blowing-suction disturbances. All these modes coexist in the boundary layer just downstream of the forcing region, which leads to the strong modulations of

pressure perturbation amplitude. Far downstream of the forcing region, acoustic modes radiate into the external flow outside the boundary layer. Mode F decays owing to its inherent stability whereas mode S grows substantially because of its instability. As a result, mode S becomes the dominant mode in the boundary layer.

5.5 Effect of location of the blowing-suction actuator

In order to investigate the effect of location of the blowing-suction actuator on receptivity, a series of numerical simulations have been carried out for different actuator locations. Specifically, seven cases of different actuator locations are considered. Fig. 16 shows a schematic of forcing actuator locations for the seven cases. In each case, wall blowing-suction with fifteen frequencies (f_n^* listed in Table 2 with n from 1 to 15) is introduced on the wedge surface. The subsequent responses of the boundary layer are simulated by the fifth-order shock-fitting finite difference method.
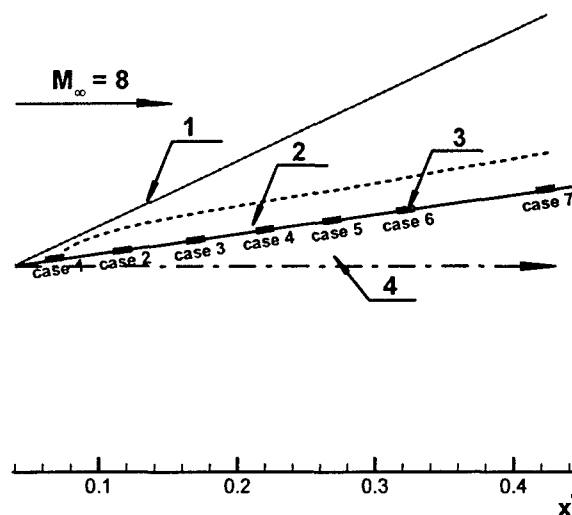

Fig. 16 A schematic of locations of the blowing-suction actuator for the seven cases: 1. bow shock; 2. boundary layer; 3. blowing-suction actuator; 4. sharp wedge.

The model of the multi-frequency blowing-suction actuator is given by Eq. (3). The constant q_0^* in model equation are different for the seven cases because it is locally defined at the leading edge of the blowing-suction actuator. The location of the forcing actuator is defined as

$$s_c^* = \frac{s_i^* + s_e^*}{2} \tag{19}$$

Constant q_0^* and other parameters of the blowing-suction actuator for the seven cases considered in

29

the current section are listed in Table 3. As already been mentioned, q^*_0 is defined at the location s_i^* as the multiple of unperturbed density on the wall and wall-normal velocity after the bow shock with the dimension of kg/m²s.

It is noticed that the relative location of the blowing-suction actuator with respect to the synchronization point plays a very important role in the receptivity process. According to Fig. 13, the synchronization point between mode F and mode S has a dimensionless circular frequency of

$\omega_s = 0.11443$. Although the synchronization point in ω coordinate does not depend on the

dimensional frequency, its location in s^* coordinate is different for different dimensional

frequency. The synchronization points in s^* coordinate for the 15 frequencies are calculated by Eq.

(14) and tabulated in Table 2 as s_{sn}^*.

Table 4 **Relative location of the blowing-suction actuator with respect to the synchronization point for the seven cases by which the effect of location of the blowing-suction actuator on receptivity is investigated**

case	$s_c^* < s_{sn}^*$	$s_c^* > s_{sn}^*$
1	n from 1 to 15	none
2	n from 1 to 12	n from 13 to 15
3	n from 1 to 10	n from 11 to 15
4	n from 1 to 9	n from 10 to 15
5	n from 1 to 8	n from 9 to 15
6	n from 1 to 7	n from 8 to 15
7	n from 1 to 6	n from 7 to 15

Table 2 shows that the synchronization point moves upstream when the dimensional frequency increases. Therefore, the blowing-suction actuators for the seven cases are located either upstream or downstream of the corresponding synchronization point of f_n^*. Table 4 lists relative locations of the blowing-suction actuators with respect to the synchronization points for the seven cases. "$s_c^* < s_{sn}^*$" represents that the forcing actuator is located upstream of the synchronization point of f_n^*, while "$s_c^* > s_{sn}^*$" represents that the blowing-suction actuator is downstream of the synchronization point of f_n^*. For example, for the dimensional frequency of $f_5^* = 74.60$ kHz, locations of the blowing-suction actuators in all cases are upstream of the synchronization point.

While for the frequency of $f_{10}^* = 149.20$ kHz, locations of the blowing-suction actuators in cases from 1 to 3 are upstream of the synchronization point, whereas locations of the blowing-suction actuators in other cases are downstream of the synchronization point.

To show the effect of location of the blowing-suction actuator on receptivity more efficiently, the perturbations of the same frequency are plotted together for the seven cases. Fig. 17 shows the pressure perturbation amplitudes of the same frequency for the seven cases of different blowing-suction locations. In these figures, the numbers of 1 to 7 within the small rectangular represent the case number. Pressure perturbation amplitudes at the frequencies f_1^*, f_2^*, and f_3^* are very small, because mode S is slightly unstable in the region upstream of the synchronization point. Therefore, pressure perturbations of these three frequencies are left out. For the frequency of $f_4^* = 59.68$ kHz, the blowing-suction actuators for all seven cases are located upstream of the synchronization point at $s_{s4}^* = 1.0618$ m. Figure (a) shows that mode S is strongly excited for all seven cases. Furthermore, the amplitudes of pressure perturbations decrease significantly when the actuator shifts from upstream to downstream. Figures (b) and (c) show similar results for pressure perturbations at the frequencies of $f_5^* = 74.60$ kHz and $f_6^* = 89.52$ kHz, respectively. At these two frequencies, Table 4 shows that the blowing-suction locations are all upstream of the corresponding synchronization points. Therefore, mode S is strongly excited for all seven cases.

When the frequency is $f_7^* = 104.44$ kHz, the location of the blowing-suction actuator is upstream of the synchronization point at $s_{s7}^* = 0.3467$ m for cases from 1 to 6, however it is downstream of the synchronization point for case 7. Figure (d) shows that mode S is strongly excited for cases from 1 to 6. In case 7, there is very little excitation of mode S, despite the fact that the blowing-suction actuator is still located within the unstable region of mode S. The results of all cases tested in this study show a consistent trend that mode S is very weakly excited when blowing-suction location is downstream of the synchronization point. For the frequency of $f_8^* = 119.36$ kHz, figure (e) shows that mode S is strongly excited for cases from 1 to 5, while there is not much excitation of mode S for case 6 and case 7. Again, this is resulted from the fact that the locations of the blowing-suction actuators for cases from 1 to 5 are upstream of the synchronization point at $s_{s8}^* = 0.2654$ m, whereas the forcing actuator is located downstream of the synchronization point for case 6 and case 7. It needs to be emphasized that the blowing-suction actuator is still located within the unstable region of mode S even in cases 6 and 7.
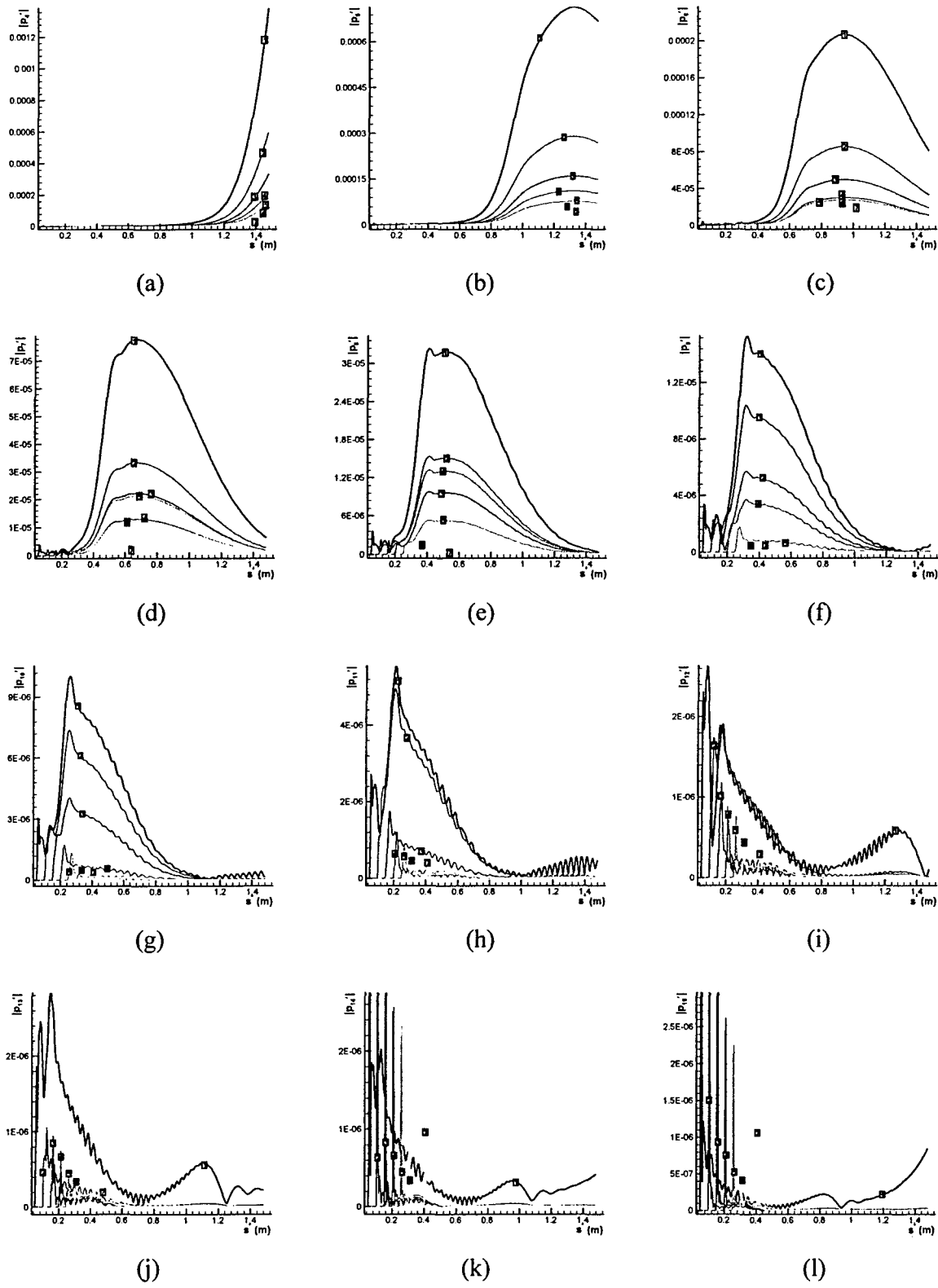
Fig. 17 Pressure perturbation amplitudes of a same frequency for the seven cases of different blowing-suction locations (f_n^* with n from 4 to 15)

As the frequency changes to $f_9^* = 134.28$ kHz in figure (f), the blowing-suction actuators are located upstream of the synchronization point at $s_{s9}^* = 0.2097$ m for cases from 1 to 4, whereas locations of the forcing actuator for cases from 5 to 7 are downstream of the synchronization point. The results for this frequency are again consistent with those of the previous frequencies regarding to the excitation of mode S. Figure (f) shows that mode S is strongly excited for cases from 1 to 4, however the excited mode S is very weak for cases from 5 to 7. For the frequencies f_n^* with n from 10 to 11, similar conclusion can be drawn. For still higher frequencies, the last three figures show that pressure perturbation is amplified in a very small domain downstream of the blowing-suction actuator, because the unstable region of mode S is small for higher frequencies. Consistently, mode S is significantly excited when the blowing-suction actuator is located upstream of the synchronization point. When the blowing-suction actuator is downstream of the synchronization point, there is a very little excitation of mode S.

To summarize, the current simulation results have consistently indicated that the synchronization point between mode F and mode S plays an important role in the excitation of mode S by the blowing-suction actuator. Mode S is strongly excited only when the blowing-suction actuator is located upstream of the synchronization point. On the other hand, when the forcing actuator is downstream of the synchronization point, there is a very weak excitation of mode S. This happens even when the blowing-suction actuator is still within the unstable region of mode S. Therefore, the synchronization point is critical to the receptivity process. The relationship between the location of the blowing-suction actuator and the synchronization point suggests that, in order to control or delay the laminar-turbulent transition more efficiently, the blowing-suction actuator should be placed upstream of the synchronization point between mode S and mode F.

6 DEVELOPMENT OF A NEW HIGH-ORDER IMMERSIED INTERFACE METHOD

Another major accomplishment of the current research project is the development of a new high-order immersed interface method. The work was motivated by discussions among the participants in the Transition Study Group Open Forum Held in the AIAA meeting in Reno in January 2005. It was pointed out that that there is a need to compute boundary layer stability and transient growth with distributive surface roughness. The new method can be arbitrarily high-order accuracy in the whole flow field, including the interface with discontinuity, and it can be useful for the simulations of transient growth to finite or nonlinear surface roughness. The new high-order immersed interface method has been tested and published in **Publications: [2], [12]**.

6.1 Introduction

Recently, there has been strong interest in developing numerical methods for computing multi-phase flow with unsteady interface. These methods have many practical applications, such as the simulation of the dynamics of gas bubbles in a liquid [29], drop deformation and breakup in viscous flow [30], free surface flow [31, 32], and the breakup of a liquid jet emanating into another fluid [33].

Compared with single-phase numerical methods, algorithms for two-phase flow simulation face additional difficulties related to the interface treatment. Firstly, the shape of the interface can be complex, and can undergo change, merge and breakup during the course of the simulation. Consequently, it is difficult to use body-fitted unsteady grid to fit the evolving interface. A fixed Cartesian grid, where the interface can cut through the grid lines, is often used. In a fixed grid, the interface can be treated by, among others, the volume-of-fluid method, the front tracking method [34, 35], the level-set method [36-39], and the boundary element method [40]. Secondly, flow variables and their derivatives can be discontinuous across the interface. Specific jump conditions at the interface depend on the physical property of the problems, the unsteadiness of the interface, and the geometric characteristics of the interface. Consequently, special treatments are necessary for computing flow equations at grid points adjacent to the interface (i.e. irregular points). One of the popular methods in treating interface discontinuity is the immersed boundary method (IBM) originally developed by Peskin [21] for simulating blood flow in the heart. The basic idea of the immersed boundary method is to model the interface by adding a delta-function source term to the Navier-Stokes equations. The resulting equations are then discretized by a standard finite difference method in a fixed Cartesian (or non-Cartesian) grid. The singular delta function is regularized by an approximate smooth function spanning a few grid cells.

An alternative to the immersed boundary method is the "sharp-interface" methods which achieve uniformly second (or higher) order accuracy by incorporating the jump conditions into the finite difference formulas. The immersed interface method (IIM) introduced by LeVeque and Li [22] is one of these methods. In presenting their original IIM method, LeVeque and Li (*1994*) considered finite difference methods for the following elliptic equation:

$$\nabla \cdot (\beta(x)\nabla u(x)) + \kappa(x)u(x) = f(x) \qquad (20)$$

The equation is defined in a simple region with a uniform Cartesian grid. Fig. 18 shows a schematic of a two-dimensional grid. There is an irregular surface Γ, which may cut across the grid lines, in the computational domain. Across the interface, β, κ, and f may be discontinuous, and along it

f may have a delta function singularity. In the derivation of finite difference formulas, the computational grid points are classified into two categories depending on their relative locations with respect to Γ: regular points away from Γ and irregular points adjacent to Γ. A globally $O(h^2)$ accuracy is achieved by using the conventional $O(h^2)$ central scheme for the regular points and a locally $O(h)$ scheme for the irregular points. In the one-dimensional case, a finite

difference formula of $O(h)$ accuracy at an irregular point uses a three-point grid stencil together with an additional correction term. A Taylor series expansion at the interface is used to obtain a set of linear equations for the undetermined coefficients and the correction term. The linear equations are often problem dependent, and they need to be solved numerically every time they are used in the simulation. In order to reach a locally $O(h)$ approximation, the correction term requires jump conditions of up to the second derivatives, i.e.

$$[u], \ [\beta u_x], \ \text{and} \ [\beta u_{xx}] \tag{21}$$

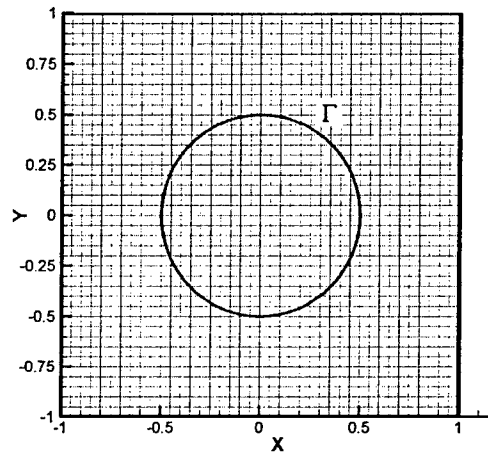where [ ] denotes the jump in variables across the interface.

Fig. 18 A schematic of two-dimensional uniform grid with an immersed interface Γ with discontinuity in solutions.

The immersed interface methods have been applied to the Stokes flow with elastic boundaries or surface tension, Hele-Shaw flow, incompressible flow based on the Navier-Stokes equations with singular source terms, and nonlinear problems in magneto-rheological fluids. Despite these applications, the immersed interface methods are often difficult to apply to complex two or three dimensional two-phase flow problems. In order to maintain a second-order accuracy, it is necessary to obtain jump conditions at the interface for flow variables and their first and second derivatives. For the Navier-Stokes equations with an interface of discontinuity, it is easy to derive the physical jump conditions for flow variables and their first derivatives across the interface. But it is difficult to obtain jump conditions for the second or high order derivatives. In order to develop third or higher order immersed interface methods, it is necessary to obtain jump conditions for the third and higher derivatives. In addition, the finite difference formulas of the original immersed interface method need to be re-derived for different problems. The coefficients and the correction terms in the

finite difference formulas at irregular points cannot be obtained explicitly. They are often computed numerically by solving a matrix equation. The repeated computations for the coefficients and correction terms can be computationally expensive.

Based on the brief review above, it is desirable for a high-order immersed interface method to have the following properties:

1. Only two physical jump conditions of the variables and their first derivatives should be needed in the second or higher order immersed interface methods.

2. Finite difference formulas at irregular points should be expressed in a general explicit form (without the need to compute matrix equations repeatedly) so that they can be applied to different problems without any modification.

The derivation, analysis, and test results of the new methods are presented in following sections. the new high-order immersed interface methods are presented in this paper for elliptic equations in the form of Eq. (20) with imbedded interface of discontinuity only. Nevertheless, the method has potential advantages in the application to two-phase flow because of its high-order accuracy and simplicity in applications by requiring only the physical jump conditions for variables and their first derivatives are needed in the finite difference formulas. The derivation of jump conditions involving the second or higher order derivatives can be difficult for two-phase flow problem involving the Navier-Stokes equations.

6.2 Explicit Finite Difference Formulas at Irregular Grid Points
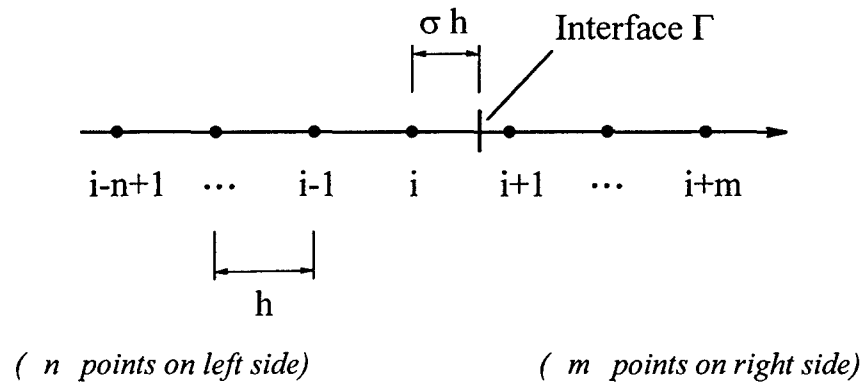

(n points on left side)   (m points on right side)

Fig. 19 Unifrom grid with an interface located on the right side of irregular point i with a general grid stencil of n and m points on the left and right sides, respectively .

The new high-order immersed interface method is presented for one-dimensional differential elliptic equations in the form of Eq. (20) in this section. The method is extended to two-dimensional elliptic equations afterward. For simplicity, only the finite difference approximation to $(du/dx)_i$ and

$(d^2u / dx^2)_i$ is presented, though formulas for higher derivatives can be easily obtained by the same method. A uniform grid of mesh size h shown in Fig. 19 is used for the discretization. Without losing generality, it is assumed that the origin of the coordinate system is located at grid point i, i.e.

$$x_{i+k} = kh \qquad (k=0, \pm1, \pm2, \cdots) \qquad (22)$$

The interface is located at:

$$x_\Gamma = x_i + \sigma h = \sigma h \qquad (23)$$

where σ is the interface location parameter which satisfies

$$0 \le \sigma \le 1 \qquad (24)$$

As discussed in the preceding section, only two jump conditions involving u and u_x are used in the finite difference approximation of the derivatives. A general jump conditions across the interface can be written as:

$$[\alpha u] = \alpha^+ u^+ - \alpha^- u^- = A \qquad (25)$$

and

$$[\beta u_x] = \beta^+ u_x^+ - \beta^- u_x^- = B \qquad (26)$$

where the superscripts, "+" and "–", represent the variables and constants at the right and left sides of the interface Γ, respectively. The constants, α^+, α^-, β^+, β^-, A, and B, are known constants determined by the nature of the equation being computed. In an actual two-phase flow problem, the jump conditions can be formulated such that α^+, α^-, β^+, β^- are dimensionless constants.

A grid point is called a regular point if the finite difference formulas at this point only involve grid points on the same side of the interface. Otherwise, it is an irregular point. If grid point i is a regular point (without the interface), finite difference approximation of an arbitrary order can be easily derived by a Taylor series expansion or by a polynomial interpolation. For example, the second and fourth order central difference approximations to $(d^2u / dx^2)_i$ are:

$$\left(\frac{d^2u}{dx^2}\right)_i = \frac{u_{i-1} - 2u_i + u_{i+1}}{h^2} + O(h^2) \qquad (27)$$

and

$$\left(\frac{d^2u}{dx^2}\right)_i = \frac{-u_{i-2} + 16u_{i-1} - 30u_i + 16u_{i+1} - u_{i+2}}{12h^2} + O(h^4) \qquad (28)$$

Therefore, in the case of $O(h^2)$ approximation in the regular points, i and $i+1$ (Fig. 19) are irregular points. For the $O(h^4)$ approximation, there are four irregular points, from $i-1$ to $i+2$. Alternatively, we can treat only points i and $i+1$ as irregular points, while 4th order one-sided approximation is used for points $i-1$ and $i+2$. The latter approach is used in this paper.

For irregular point i shown in Fig. 19, the use of Eq. (27) will lead to large computational errors because of the discontinuity of u at Γ. LeVeque and Li [22] derived a locally $O(h)$ approximation at i by adding a correction term to the three-point stencil. The difference formula and the correction term are then determined by a Taylor expansion at the interface. In order to reach $O(h)$ approximation, it is necessary to know the jump conditions involving u, u_x and u_{xx}. The first two jump conditions can be obtained easily. The jump conditions for the second derivatives can be obtained by taking derivatives of the lower order jump conditions together with the differential equation.

Therefore, the high-order immersed interface method presented below achieves a high-order approximation at the irregular point i by imposing the two jump conditions given by Eqs. (25) and (26) only. Instead of using more and more jump conditions of higher order derivatives to achieve higher order accuracy at the irregular point as done in the original IIM method, we use more and more grid points on both sides of the interface so that arbitrary order approximation can be achieved while only the two jump conditions (25) and (26) are imposed. General difference formulas for $(du/dx)_i$ and $(d^2u/dx^2)_i$ in explicit form can be derived by a matched polynomial expansion, so that they are problem independent.

Finite difference approximation for $(du/dx)_i$ and $(d^2u/dx^2)_i$ at the irregular point i is considered by using a stencil of n points on the left of Γ and m points on the right (Fig. 2). The order of the approximation increases with the increasing values of n and m. In order to have a uniform accuracy, it is desirable to have the same number of points on both sides of the interface, i.e.

$$n = m \qquad (29)$$

Since n and m can be different in some special circumstances, we derive the general formulas by assuming arbitrary values of n and m. The finite difference formulas for i can be derived by a Taylor series expansion with σ as a parameter. The case of locally $O(h)$ approximation for $(d^2u/dx^2)_i$ at interface is considered first as an example below. A general formula for arbitrary

values of n and m is derived afterward.

6.3 Test and applications

The new method can be of arbitrarily high-order accuracy and it is simple to be applied to practical two-phase flow problems by requiring only the physical jump conditions for variables and first derivatives. It also has the advantage that the finite difference formulas at irregular points are expressed in an explicit form so that they can be applied to difference problems without modifications. Six versions of the new method of up to fourth order accuracy have been tested for both one and two-dimensional model equations. The numerical results show that they can produce very accurate results for elliptic equations with embedded interfaces. Details of test results have been published in **Publications: [2], [12]**.

7 PERSONNEL

The following personnel conduct research for the grant and are partially supported by the grant:

1. Professor Xiaolin Zhong, principal investigator.

2. Xiaowen Wang, a Ph.D. student. He will graduate with a Ph.D. degree in May 2007.

3. Pradeep S. Rawat, a Ph.D. student.

8 PUBLICATIONS

The following publications are completed from work supported by this grant:

In Journals or Book Chapters:

1   R. K. Shukla and X. Zhong, "Very high-order compact finite difference schemes on non-uniform grids for incompressible Navier-Stokes equations," accepted for publication by the Journal of Computational Physics, November 2006.

2   X. Zhong "A new high-order immersed interface method for solving elliptic equations with imbedded interface of discontinuity" **Journal of Computational Physics**, Available online 30 January 2007.

3   A. Tumin, X. Wang, and X. Zhong "Direct numerical simulation and the theory of receptivity in a hypersonic boundary layer," **Physics of Fluids**, Vol. 19, Paper No. 014101, 2007.

4   X. Zhong and Y. Ma "Boundary-layer receptivity of Mach 7.99 Flow over a blunt cone to free-stream acoustic waves," **Journal of Fluid Mechanics**, Vol. 556, pp. 55-103, 2006.

5   Y. Ma and X. Zhong "Receptivity of a supersonic boundary layer over a flat plate. Part 3: effects of different types of free-stream disturbances," **Journal of Fluid Mechanics**, Vol. 532, pp. 63-109, 2005.

6   R. K. Shukla and X. Zhong "Derivation of high-order compact finite difference schemes for non-uniform grid using polynomial interpolation," **Journal of Computational Physics**, Vol. 204, pp. 404-429, 2005.

7   A. Tumin, X. Wang, and X. Zhong "DNS and the theory of receptivity in a hypersonic boundary layer," **Bulletin of the American Physical Society**, Vol. 50, No. 9, pp. 180, 2005.

8   J. J. Yoh and X. Zhong "New Hybrid Runge-Kutta Methods for Unsteady Reactive Flow Simulation," **AIAA Journal**, Vol. 42, No. 8, pp. 1593-1600, 2004.

9   J. J. Yoh and X. Zhong "New Hybrid Runge-Kutta Methods for Unsteady Reactive Flow Simulation: Applications," **AIAA Journal**, Vol. 42, No. 8, pp. 1601-1611, 2004.

In Conference Proceedings:

10 X. Wang and X. Zhong "Numerical simulation of hypersonic boundary-layer receptivity to two and three-dimensional wall perturbations," **AIAA paper 2007-0946**, January 2007.

11 X. Wang and X. Zhong "Numerical simulation of hypersonic boundary-layer receptivity to three-dimensional wall perturbations," **AIAA paper 2006-3225**, June 2006.

12 X. Zhong "A new high-order immersed interface method for multi-phase flow simulation," **AIAA paper 2006-1294**, January 2006.

13 X. Wang and X. Zhong "Numerical simulation and experiment comparison of leading-edge receptivity of a Mach 5.92 boundary layer," **AIAA paper 2006-1107**, January 2006.

14 A. Tumin, X. Wang, and X. Zhong "Direct numerical simulation and the theory of receptivity in a hypersonic boundary layer," **AIAA paper 2006-1108**, January 2006.

15 X. Zhong "Effect of nose bluntness on hypersonic boundary layer receptivity over a blunt cone," **AIAA paper 2005-5022**, June, 2005.

16 X. Wang and X. Zhong "Receptivity of a Mach 8 flow over a sharp wedge to wall blowing-suction," **AIAA paper 2005-5025**, June 2005.

17 P. S. Rawat, X. Zhong, V. Singh, and S. Gogineni "Numerical simulation of secondary flow in a weakly ionized supersonic flow with applied electromagnetic field," **AIAA paper 2005-5050**, June, 2005.

18 X. Zhong "Numerical simulation and experimental comparison of hypersonic boundary layer instability over a blunt cone," **AIAA paper 2004-2244**, June 2004.

19 V. Singh, X. Zhong, and S. Gogineni "Numerical simulation of supersonic boundary layer stability with applied electromagnetic field in a weakly ionized flow," **AIAA 2004-2724**, 2004.

20 Y. Ma and X. Zhong, "Receptivity to freestream disturbances of a Mach 10 nonequilibrium reacting oxygen flow over a flat plate," **AIAA paper 2004-0256**, January 2004.

21 X. Wang and X. Zhong "Receptivity of a supersonic boundary layer over a sharp wedge to wall blowing/suction," **AIAA paper 2004-0254**, January 2004.

22 X. Zhong "Receptivity of Mach 6 flow over a flared cone to freestream disturbances," **AIAA paper 2004-0253**, January 2004.

Ph.D. Thesis:

23 X. Wang "Numerical Simulations of Supersonic Boundary-Layer Stability and Receptivity," Ph.D. Thesis, Mechanical Engineering, UCLA, 2007.

9 ACKNOWLEDGEMENT / DISCLAIMER

10 REFERENCES

1. Zhong, X., *High-Order Finite-Difference Schemes for Numerical Simulation of Hypersonic Boundary-Layer Transition*. Journal of Computational Physics, 1998. **144**: p. 662-709.

2. Tumin, A., Wang, X., and Zhong, X., *Direct Numerical Simulation and the Theory of*

Receptivity in a Hypersonic Boundary Layer Physics of Fluids, 2007. **19**: p. Paper No. 014101.

3. Wang, X., and Zhong, X., *Receptivity of a Mach 8 Flow over a Sharp Wedge to Wall Blowing-Suction.* AIAA paper 2005-5025, 2005.

4. Wang, X., and Zhong, X., *Numerical Simulation and Experiment Comparison of Leading-Edge Receptivity of a Mach 5.92 Boundary Layer.* AIAA paper 2006-1107, 2006.

5. Wang, X., and Zhong, X., *Numerical simulation of hypersonic boundary-layer receptivity to two and three-dimensional wall perturbations.* AIAA paper 2007-0946, 2007.

6. Zhong, X., and Ma, Y., *Boundary-layer receptivity of Mach 7.99 Flow over a blunt cone to free-stream acoustic waves.* Journal of Fluid Mechanics, 2006. **556**: p. 55-103.

7. Zhong, X., *Effect of Nose Bluntness on Hypersonic Boundary Layer Receptivity over a Blunt Cone.* AIAA paper 2005-5022, 2005.

8. Zhong, X., *Numerical Simulation and Experimental Comparison of Hypersonic Boundary Layer Instability over a Blunt Cone.* AIAA paper 2004-2244, 2004.

9. Stetson, K.F., Thompson, E. R., Donaldson, J. C., and Siler, L. G., *Laminar Boundary Layer Stability Experiments on a Cone at Mach 8, Part 2: Blunt Cone.* AIAA paper 84-0006, 1984.

10. Maslov, A.A., Shiplyuk, A. N., Sidorenko, A., and Arnal, D., *Leading-edge Receptivity of a Hypersonic Boundary Layer on a Flat Plate.* Journal of Fluid Mechanics, 2001. **426**: p. 73-94.

11. Zhong, X. *A New High-Order Immersed Interface Method for Multi-Phase Flow Simulation.* in *AIAA paper 2006-1294.* 2006.

12. Zhong, X., *A New High-Order Immersed Interface Method for Solving Elliptic Equations with Imbedded Interface of Discontinuity* Journal of Computational Physics, 2007. **doi: 10.1016/j.jcp.2007.01.017.**

13. Zhong, X., *Leading-Edge Receptivity to Free Stream Disturbance Waves for Hypersonic Flow over a Parabola.* Journal of Fluid Mechanics, 2001. **441**: p. 315-367.

14. Schneider, S.P., *Hypersonic Laminar-Turbulent Transition on Circular Cones and Scramjet Forebodies.* Progress in Aerospace Sciences, 2004. **40**: p. 1-50.

15. Malik, M.R., Lin, R. S., and Sengupta, R., *Computation of Hypersonic Boundary-Layer*

Response to External Disturbances. AIAA paper 1999-0411, 1999.

16. Ma, Y., and Zhong, X., *Receptivity to Freestream   Disturbances of Mach 8 Flow over A Sharp Wedge.* AIAA paper 2003-0788, 2003.

17. Tumin, A., Wang, X., and Zhong, X., *Direct Numerical Simulation and the Theory of Receptivity in a Hypersonic Boundary Layer.* AIAA paper 2006-1108, 2006.

18. Reshotko, E., *Transient growth: a factor in bypass transition.* Physics of Fluids, 2001. **13**: p. 1067-1075.

19. Reshotko, E., and Tumin, A., *Spatial theory of optimal disturbances in boundary layers.* Physics of Fluids, 2001. **13**(7): p. 2097-2104.

20. Reshotko, E., and Tumin, A., *Role of Transient Growth in Roughness-Induced Transition.* AIAA Journal, 2004. **42**(4): p. 766-771.

21. Peskin, C., *The immersed boundary method.* Acta Numerica, 2002: p. 479-527.

22. LeVeque, R., and Li, Z., *The immersed interface method for elliptic equations with discontinuous coefficients and singular sources.* SIAM Journal of Numerical Analysis, 1994. **31**: p. 1001-1025.

23. Fedorov, A.V., and Khokhlov, A. P., *Receptivity of Hypersonic Boundary Layer to Wall Disturbances.* Theoretical and Computational Fluid Dynamics, 2002. **15**: p. 231-254.

24. Eibler, W., and Bestek, H., *Spatial Numerical Simulations of Linear and Weakly Nonlinear Instabilities in Supersonic Boundary Layers.* Theoretical and Computational Fluid Dynamics, 1996. **8**: p. 219-235.

25. Egorov, I.V., Fedorov, A. V., and Soudakov, V. G. , *Direct Numerical Simulation of Unstable Disturbances in Supersonic Boundary Layer.* AIAA paper 2004-0588, 2004: p. 1-11.

26. Ma, Y., and Zhong, X., *Receptivity to Freestream Disturbances of a Mach 10 Nonequilibium Reacting Oxygen Flow over a Flat Plate.* 2004. **AIAA 2004-0256**.

27. Malik, M.R., *Numerical methods for hypersonic boundary layer stability.* Journal of Computational Physics, 1990. **86**: p. 376-413.

28. Ma, Y., and Zhong, X., *Receptivity of a Supersonic Boundary Layer over a Flat Plate. Part 1: Wave Structures and Interactions.* Journal of Fluid Mechanics, 2003. **488**: p. 31-78.

43

29. Feng, Z.C., and Leal, L. G, *Nonlinear bubble dynamics.* Annual Review of Fluid Mechanics, 1997. **29**: p. 201-243.

30. Stone, H.A., *Dynamics of drop deformation and breakup in viscous fluids.* Annual Review of Fluid Mechanics, 1994. **26**(65-102).

31. Tsai, W., and Yue, D. K, *Computation of nonlinear free-surface flows.* Annual Review of Fluid Mechanics, 1996. **28**(249-278).

32. Scardovelli, R., and Zaleski, S., *Direct numerical simulation of free-surface and interfacial flow.* Annual Review of Fluid Mechanics, 1999. **31**: p. 567-603.

33. Lin, S.P., and Reitz, R. D., *Drop and spray formation from a liquid jet.* Annual Review of Fluid Mechanics, 1998. **30**: p. 85-105.

34. Tryggvasson, G., Bunner, B., Esmaeeli, A., Juric, D., Al-Rawahi, N., Tauber, W., Han, J., Nas, S., and Jan, Y.-J. , *A Front-Tracking Method for the Computations of Multiphase Flow.* Journal of Computational Physics, 2001. **169**: p. 708-759.

35. Glimm, J., et al., *A 2001 Critical Analysis of Rayleigh-Taylor Growth Rates.* Journal of Computational Physics, 2001. **169**: p. 652-677.

36. Sethian, J.A., *Level Set Methods and Fast Marching Methods.* Cambridge University Press, 1999: p. Cambridge, UK.

37. Sethian, J.A., *Evolution, Implementation, and Application of Level Set and Fast Marching Methods for Advancing Fronts.* Journal of Computational Physics, 2001. **169**: p. 503-555.

38. Osher, S., and Fedkiw, R., *Level Set Methods: An Overview and Some Recent Results.* Journal of Computational Physics, 2001. **169**: p. 463-502.

39. Osher, S., and Fedkiw, R., *Level Set Methods and Dynamic Implicit Surfaces.* 2003, New York: SpringerVerlag.

40. Pozrikidis, C., *Interfacial Dynamics for Stokes Flow.* Journal of Computational Physics, 2001. **169**: p. 259-301.